Surface Composition Dependent Ligand Effect in Tuning the Activity of Nickel-copper Bimetallic Electrocatalysts towards Hydrogen Evolution in Alkaline

Chao Wei,[†,∟,Δ] Yuanmiao Sun,[†,Δ] Günther G. Scherer,[‡,§] Adrian C. Fisher,[‖] Matthew Sherburne,[▽] Joel W. Ager,[▽] Zhichuan J. Xu*[,†,∟,⊥]

[†]School of Materials Science and Engineering, Nanyang Technological University, 50 Nanyang Avenue, 639798, Singapore;

[‡]Department for Management of Science and Technology Development, Ton Duc Thang University, Ho Chi Minh City, Vietnam;

[§]Faculty of Applied Sciences, Ton Duc Thang University, Ho Chi Minh City, Vietnam;

[‖]Department of Chemical Engineering, University of Cambridge, Cambridge CB2 3RA, UK;

[▽]Department of Materials Science and Engineering, University of California at Berkeley, Berkeley, California 94720, USA

[∟]Solar Fuels Laboratory, Nanyang Technological University, 50 Nanyang Avenue, 639798, Singapore;

[⊥]Energy Research Institute @ Nanyang Technological University, 50 Nanyang Avenue, 639798, Singapore

KEYWORDS: electrocatalysis, alkaline hydrogen evolution reaction, d band center, bimetallic catalysts

ABSTRACT: Exploring efficient and low-cost electrocatalysts for hydrogen evolution reaction (HER) in alkaline media is critical for developing anion exchange membrane electrolyzers. The key to a rational catalyst design is understanding the descriptors that govern the alkaline HER activity. Unfortunately, the principles that governs alkaline HER performance remain unclear and are still under debate. By studying the alkaline HER at a series of NiCu bimetallic surfaces, where the electronic structure is modulated by ligand effect, we demonstrate that alkaline HER activity can be correlated with either the calculated or the experimental-measured d band center (an indicator of hydrogen binding energy) via a volcano-type relationship. Such correlation indicates the descriptor role of d band center, and this hypothesis is further supported by the evidence that combining Ni and Cu produces a variety of adsorption sites, which possess near-optimal hydrogen binding energy. Our finding broadens the applicability of d band theory to activity prediction of metal electrocatalysts and may offer an insightful understanding of alkaline HER mechanism.

Introduction

The transition of the energy infrastructure from fossil fuels to sustainable energy sources requires us to develop low-cost energy storage and conversion technologies that utilize renewable energy (such as solar, tidal, wind, etc.) for providing electricity at-scale and on-demand.[1-3] A promising method is to electrochemically generate H_2 as an energy carrier.[4] Energy is stored by electrochemical water splitting, which produces H_2 and O_2; and their recombination, for example, can generate electricity via fuel cells.[1, 5-6] To realize this hydrogen-based energy system, one of the key challenges is to efficiently produce H_2. This challenge requires the use of highly active and cost-effective catalysts to minimize the overpotential necessary for driving the hydrogen evolution reaction (HER), which constitutes half of the water splitting process. Platinum is the state-of-the-art catalyst for HER in acid electrolyte, but the scarcity and high cost of platinum limits its widespread technological usage, and thus calling for the search for highly active, earth-abundant catalysts to replace Pt.[7-8]

The alkaline environment of hydroxide exchange membrane enables the possibility of using non-precious metal catalysts for HER.[9-11] To guide the rational search for metal HER catalysts in alkaline, researchers have established some design principles, such as the hydrogen binding energy theory.[9, 12-13] Despite the recent evidences about the role of adsorbed OH in the water dissociation step for HER in alkaline,[14-16] hydrogen binding energy has been proved to be the dominant factor that governs alkaline HER activity at various monometallic catalysts.[9, 12-13, 17] Inspired by the success of hydrogen binding energy, we further infer that alkaline HER at metal catalysts is governed by the position of d band center, because adsorbate binding energy (e.g. hydrogen binding energy) is usually reflected by the d band center, which has been universally accepted as the descriptor for HER in acid;[18-20] and also other catalysis reactions.[21-24]

There are several works that attempt to raise the community's awareness of the importance of d band center to alkaline HER at sulfide,[25] phosphide,[26] nitride[27] and metal catalysts.[28-31] Despite the pioneering efforts, there is still a lack of a systematic study that tunes the d band center over a broad range and identifies an optimum value (Sabatier principle)[32] by directly establishing the relationship of alkaline HER activity vs. d band center. The absence of this relationship leads to the circumstance that the applicability of d band theory to alkaline HER is unanswered and the role of the d band center position in alkaline HER at metal catalysts remains elusive. Acquiring such knowledge is helpful for broadening our fundamental understanding on alkaline HER and instructing the design of more efficient electrocatalysts for alkaline HER.

To address this issue, this article chooses a series of NiCu bimetallic nanoparticles (NPs) as the model material to study the correlation between alkaline HER activity and the position of d band center. NiCu is chosen because alkaline HER at Ni-[33-35] and Cu-based[36] non-precious metals has exhibited excellent activity (even approaches Pt), which deserves more studies for further activity improvement. We synthesized NiCu NPs via a colloidal method. By varying the surface compositional ratio of Ni to Cu, we took the advantage of ligand effect[20, 37] - the metal ligands of the surface atoms are changed - to tune the position of d band center, which is quantified by density functional theory (DFT) calculation and X-ray photoelectron spectroscopy (XPS) measurement. The intrinsic HER activity of NiCu bimetallic surface exhibits a volcano-shaped dependence on the d band position, which indicates that the d band center can be primarily used as a descriptor for alkaline HER. The applicability of d band center is further supported by the evidence that combination of Ni and Cu produces a variety of adsorption sites, which possess near-optimal hydrogen binding energy.

Methods

Synthesis of NiCu nanoparticles (NPs). The free-standing NiCu NPs with various compositions were synthesized by reducing $Ni(acac)_2$ and $Cu(acac)_2$ in oleylamine. In a typical synthesis of Ni_1Cu_1 NPs, 0.5 mmol $Ni(acac)_2$, 0.5 mmol $Cu(acac)_2$, 10 ml oleylamine and 0.8 ml oleic acid were mixed at room temperature (25 °C). The solution was then kept at 120 °C under an Ar blanket for 30 min to remove the moisture. Then the solution was heated to 220 °C at a heating rate of 2 °C/min. The reaction was maintained at 220 °C for 1 hr and then naturally cooled down to room temperature. As-prepared Ni_1Cu_1 NPs were collected and washed by centrifugation. The composition was varied by changing the precursor ratio between $Ni(acac)_2$ and $Cu(acac)_2$.

Carbon loading. A suspension of Vulcan XC-72 (Premetek, USA) was prepared by sonicating ~320 mg of Vulcan in 600 ml hexane in an ice bath for 5 hours. Afterward, a suspension of as-prepared NiCu NPs in hexane was added into the Vulcan suspension and the mixture was further sonicated for 2 additional hours. The catalyst powders were collected by purging Ar (evaporating hexane) at room temperature and dried in vacuum oven for 24 hr. The mass loading of NiCu NPs at NiCu/C catalysts was controlled at 20 w%. To remove the surfactants attached on NPs, the NiCu/C catalysts were heated up to 250 °C under air and maintained at this temperature for 30 min. After naturally cooling down to the room temperature, the air atmosphere was switched to a mixture of H_2/Ar (5% H_2) and the temperature was further increased up to 200 °C and maintained for 1 hr.

Physical characterization. The TEM study was carried out on a JEOL 2010 transmission electron microscope at 200 kV. The X-ray diffraction pattern was collected on a PANalytical X'pert Pro with Cu Kα radiation (λ =1.5418 Å). The XRD samples were prepared by dropping highly concentrated NP solution onto glass slides. The composition of NPs was determined by ICP. For X-ray photoelectron spectroscopy (XPS) experiments a PHI5700 spectrometer, made by Physical Electronics, was employed.

Electrochemical measurement. Working electrodes were fabricated by drop-casting catalysts onto glassy carbon rotating disk electrode (RDE) with a modified ink recipe as described previously.[6] The as-prepared NiCu/C catalysts were dispersed in a mixture of solvents containing water, isopropanol and Nafion® perfluorinated resin solution (5 wt% in water) (v/v/v = 4/1/0.04). After sonicating for 1 hr in an ice bath, 15 μL of this ink was then dropped onto the glassy carbon RDE electrode (5 mm diameter) and dried at room temperature, yielding a metal mass loading of 2 μg_{metal} (10.2 $\mu g_{metal}/cm^2_{disk}$). HER tests were conducted in a three-electrode cell, where the working electrode compartment and counter electrode compartment were separated by an AMI-7001 anion exchange membrane (Figure S17). Electrochemical data was recorded by a BioLogic SP-150 potentiostat at room temperature (25 °C). A Pt foil served as counter electrode and a mercury-mercury oxide (Hg/HgO, filled with 0.1 M KOH solution) was used as reference electrode. The HER performance was assessed by the cyclic voltammetry (CV) at 10 mV/s with a rotation speed of 1600 rpm in H_2-saturated 0.1 M KOH (prepared by Sigma-Aldrich potassium hydroxide, assay 99.99%). The applied potentials were converted to the RHE scale via reference electrode calibration in H_2-saturated 0.1 M KOH. The potentials were further iR-corrected. R (the uncompensated resistance) was measured by electrochemical impedance spectroscopy (EIS). The ECSA of Ni was extracted based on the Coulombic charge under the OH adsorption peak at 0.2 V vs. RHE,[38] and ECSA of Cu was measured by the charge under the peak (at 0.6 V vs RHE) which represents the formation of Cu_2O monolayer. See the detailed methodology discussion in Supporting Information (SI).[9]

DFT calculation. All DFT calculations were performed by using Vienna Ab-initio Simulation Package (VASP) under the Projected Augmented Wave (PAW) method. The revised Perdew-Burke-Ernzerhof (RPBE) functional was used to describe the exchange and correlation effects, since it has been proved to provide useful trend in computing adsorption energies.[39-40] In all the calculations, the cutoff energy was set to be 450 eV. The (111) surface was used to represent the catalytic interface of the metals and metal alloys. The Monkhorst-Pack grids[41] were set to be 4×4×1 and 9×9×1 for computing the surface optimizations and density of states (DOS) calculations, respectively. At least 18 Å vacuum layer was applied in z-direction of the slab models, preventing the slabs from vertical interactions. The descriptor proposed by Norskov et al. was used to describe the HER activity on a given catalyst surface, where the free energy of hydrogen adsorption (ΔG_{H^*}) was considered as the key parameter determining the HER activity.[42] For HER in aqueous solutions, it is a two-step process and involves only one reaction intermediate, the chemisorbed H atom. The free energy of the adsorbed hydrogen is defined as: $\Delta G_{H^*} = \Delta E_H + \Delta E_{ZPE} - T\Delta S_H$, where ΔE_H is the hydrogen binding energy, ΔE_{ZPE}

is the zero-point energy difference between adsorbed hydrogen and gaseous hydrogen, and TΔS is the corresponding entropy difference between these two states. According to previous studies,[42] here we used 0.24 eV to represent the correction of zero point energy and entropy of hydrogen state.

Preparation of NiCu bimetallic catalysts

A series of NiCu NPs were consistently synthesized by the same colloidal route (which is modified from a literature approach),[43] and the composition ratio was controlled by varying the feeding ratio of Ni to Cu precursors. Transmission electron microscopy (TEM) imaging (Figure S1) reveals that the as-synthesized NiCu NPs are spherical. X-ray diffraction (XRD) patterns show typical fcc crystal phases with diffraction peaks between the standard Ni and Cu peaks (Figure 1), indicative of polycrystalline NiCu solid solutions, which is consistent with the XRD analysis on NiCu alloys reported previously.[44-45] To avoid NPs aggregation in later electrocatalysis tests,[43] these free-standing NiCu NPs were loaded onto a supporting material, i.e. Vulcan carbon, by long-term sonication to yield NiCu/carbon (denoted as NiCu/C) catalysts, where the weight percentage of metal is 20 wt%. The surface of NPs synthesized by colloidal methods is usually attached with surfactant molecules, which might interfere with the electrocatalytic activity measurement.[46] Thus, to rule out such interference, the NiCu/C catalysts were heat-treated in air for surfactant removal,[46] followed by heat-treatment in a reducing atmosphere, i.e. 5% H_2/Ar, to ensure the catalysts are metallic. After this two-step heat-treatment, the XRD patterns confirm that the NPs are still solid solutions (Figure S2); and the grain sizes (Figure S3h) obtained from Scherrer equation analysis of XRD (111) peaks indicate these NPs are polycrystalline. The consistency between the nominal feeding ratio of precursors and bulk composition ratio of NPs is confirmed by Inductively Coupled Plasma (ICP, Figure S4). TEM shows that they are spherical (Figure 1, S5-S9) without specific orientation. To know the exposed facet and strain, the TEM-based surface analysis was performed (examples in Figure S5-S9). The statistical results (Figure S10) show that the surfaces of these NiCu/C particles consistently have a dominant preference for (111), indicating that the facet exposure is not a variable across NiCu bimetallic catalysts with different compositions; in addition, strain was not observed at these catalysts. The exemplary energy-dispersive X-ray spectroscopy (EDS) mapping at various NiCu/C (Figure S11) visualizes that increasing the bulk concentration of Ni leads to the transition from Cu-rich to Ni-rich surface (further quantified by electrochemistry measurement in the next section). By counting >250 particles,[47] the statistical average sizes of NiCu NPs (at NiCu/C after heat-treatment) are shown in Figure S3. The size histograms indicate that, at NiCu/C catalysts, NiCu NPs with various compositions have comparable particle sizes, which rules out a size effect on the later HER studies.[48] Hereafter, the resulting heat-treated NiCu/C catalysts are used for the following electrochemistry tests. As control experiments, pure Ni/C and Cu/C catalysts were also prepared by the same procedures.

Surface composition of NiCu bimetallic catalysts

Since the surface region (rather than the bulk NP) directly governs the electrocatalytic performance, we quantify the surface composition and surface area of these NiCu/C catalysts. To measure the surface composition, cyclic voltammetry (CV) – a surface-sensitive technique – was performed by referencing a well-published literature methodology.[9] As revealed in both literature and our results, either Ni or Cu does not show the characteristic CV peaks of H adsorption/desorption,[9, 38, 49-50] which is a standard method for quantifying the electrochemical active surface area (ECSA) of Pt catalysts. The ECSA of Ni was extracted based on the Coulombic charge under the OH adsorption peak at 0.2 V vs. RHE,[9, 38, 49] and ECSA of Cu was measured by the charge under the peak (at 0.6 V. vs RHE) which represents the formation of a Cu_2O monolayer (see the detailed methodology discussion in SI).[9, 50] It can be qualitatively observed that as the bulk Ni composition increases, the intensity of the CV peak that signifies surface Ni increases, and that for Cu decreases (Figure 2 and S12), indicating that these NiCu/C catalysts possess different surface composition. This observation is fundamentally the same as a CV study at PtAu NPs, where a larger Pt coverage at surface gives a larger peak that represents surface Pt and a smaller peak for Au. The

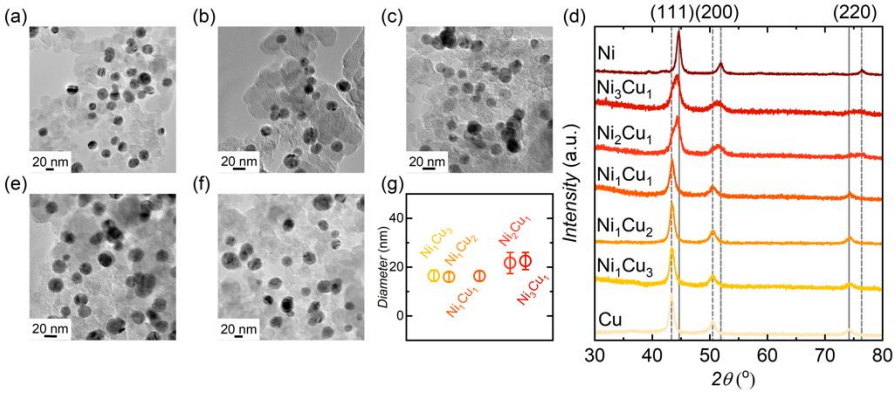

Figure 1. Transmission electron microscopy (TEM) images of NiCu nanoparticles (NPs) loaded on carbon (NiCu/C, after heat treatment) with different nominal compositions: (a) Ni_1Cu_3/C, (b) Ni_1Cu_2/C, (c) Ni_1Cu_1/C, (e) Ni_2Cu_1/C, (f) Ni_3Cu_1/C. (d) X-ray diffraction (XRD) patterns at free-standing NiCu NPs with different nominal compositions: Ni_1Cu_3, Ni_1Cu_2, Ni_1Cu_1, Ni_2Cu_1, Ni_3Cu_1. The vertical dash lines are standard Cu and Ni XRD patterns extracted from PDF No. 03-065-9026 and PDF No. 03-065-0380, respectively. (g) The average diameter of NiCu NPs measured from > 250 NPs at TEM images.

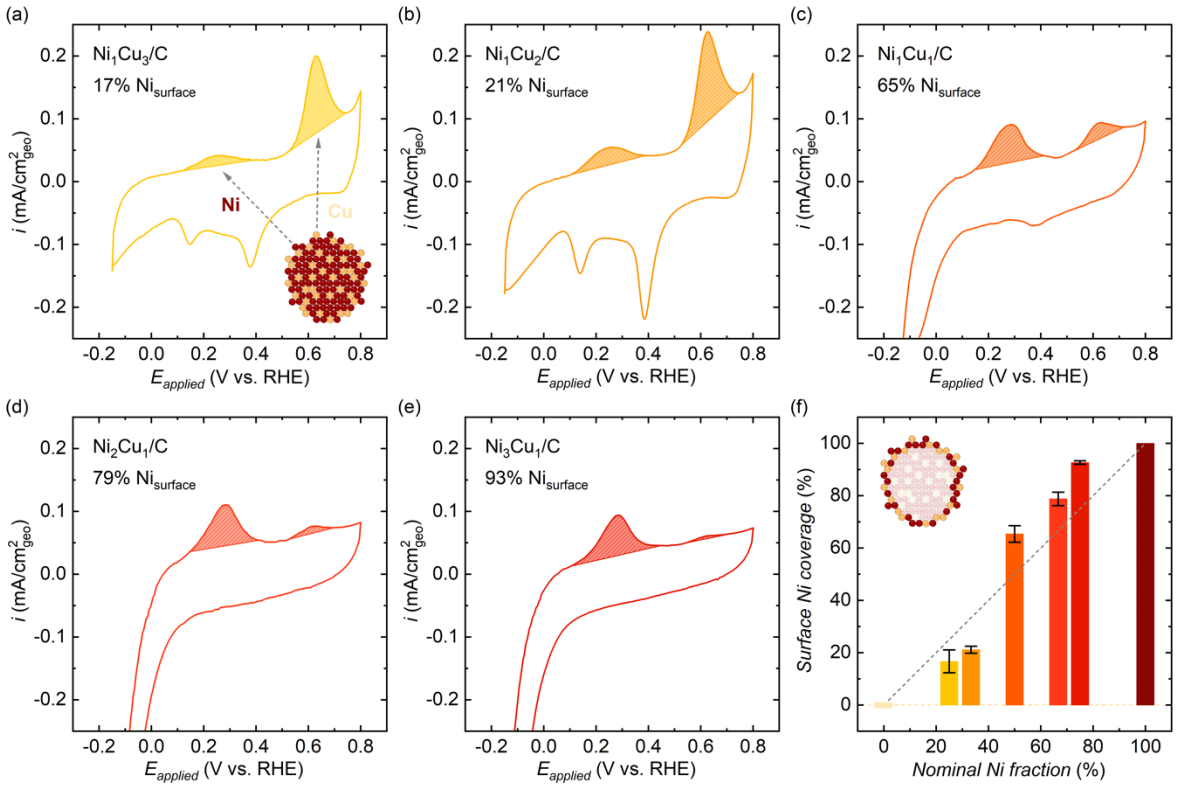

Figure 2. Cyclic voltammetries (CVs) of NiCu nanoparticles (NPs) supported on carbon (NiCu/C) with different nominal compositions, (a) Ni_1Cu_3/C, (b) Ni_1Cu_2/C, (c) Ni_1Cu_1/C, (d) Ni_2Cu_1/C, (e) Ni_3Cu_1/C. CVs were collected in Ar-saturated 0.1 M KOH at the scan rate of 20 mV/s. (f) The surface Ni coverage versus bulk fraction of Ni. The surface Ni coverage was estimated by CV-derived electrochemical active surface area (ECSA). The dash line represents the surface Ni coverage equals bulk fraction of Ni. The error bars represent at least three independent measurements.

variation of the CV peaks for Ni and Cu at our various NiCu catalysts indicates that these peaks are sensitive to the surface composition, and thus the ECSA can be reliably determined by these peaks. To quantify the surface composition, we use Ni coverage, which is defined as the surface fraction of Ni. Plotting Ni coverage against NPs bulk composition shows that, with a larger fraction of bulk Ni, the surface Ni coverage increases; and the surface Ni coverage slightly differs from the bulk.

To supplement the ECSA-derived surface composition, XPS is additionally employed to measure the Ni fraction, which is estimated according to the integrated areas of the Ni 2p region from 850 to 890 eV[34] and the Cu 2p region from 925 to 960 eV (Figure S13 and S14).[45] Figure S15 reveals that the Ni fraction derived from XPS agrees well with that obtained by ECSA, indicating that our ECSA method is indeed able to reflect the surface composition. Considering that XPS does not necessarily probe the outmost surface layer (even the angle-dependent XPS is difficult for powders),[51] we choose ECSA-derived Ni fraction for further discussion. The surface areas of catalysts (i.e. the surface areas of NiCu NPs at NiCu/C), which will be used for extracting HER intrinsic activities in the next section, were estimated by totalling ECSA of Ni and Cu (Figure S16). As a reference, we also present the surface areas estimated by TEM with a spherical approximation (see method in SI and results in Figure S16).[47] The TEM-derived surface area is slightly larger than ECSA, which has also been reported in previous studies on Pt NPs.[52] This discrepancy between these two methods might be due to the fact that the contact area between NPs and the carbon support is included in TEM analysis but is inaccessible in CV measurement.[52] Thus we choose ECSA for the following intrinsic activity analysis.

HER intrinsic activities of NiCu bimetallic catalysts in alkaline

The NiCu/C catalysts with various Ni fraction possess different HER intrinsic activities (surface-area-normalized activities) in alkaline. The alkaline HER activity of NiCu/C catalysts was measured by CV in H_2-saturated 0.1 M KOH electrolyte and the working electrodes were prepared by the traditional drop-casting method.[4, 6] The working electrode compartment and counter electrode compartment were separated by an anion exchange membrane to avoid Pt contamination from Pt counter electrode (Figure S17). Geometric current densities (current normalized to the geometric area of glassy carbon disk) of NiCu/C catalysts with various surface composition show different overpotentials to reach the current density of 1 mA/cm^2_{disk}, varying from ~590 mV for Cu/C to ~160 mV for Ni_2Cu_1/C (Figure S18). Because the activity based on geometric current density does not reflect the intrinsic chemistry of a given electrocatalyst, we next discuss the specific activity, which reflects the intrinsic activity. The critical role of specific activity in analysing intrinsic activity can be found in the published literature.[1, 5-6, 47, 53]

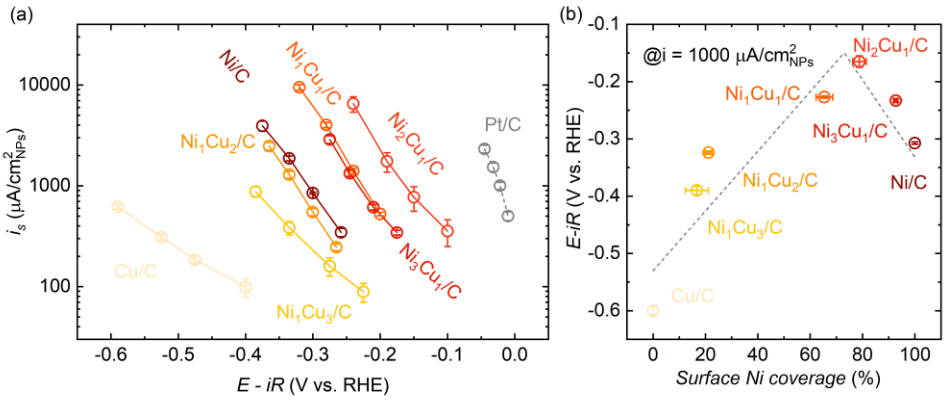

Figure 3. (a) Hydrogen evolution reaction (HER) specific activities, i_s, of various NiCu/C catalysts obtained after background-correction (by averaging the positive- and negative-going scans of cyclic voltammetry, which was collected with a scan rate of 10 mV/s and a rotation speed of 1600 rpm in H_2-saturated 0.1 M KOH at 25 °C) and iR-correction. The current density is normalized to the surface area of NiCu bimetallic catalysts. Note the specific activity of Pt/C is the nominal activity, which is obtained by normalizing the measured current density to the surface area Pt. (b) HER specific activity of various NiCu/C catalysts as a function of surface Ni coverage. The specific activity is defined as the potential at 1000 $\mu A/cm^2_{NPs}$, which is the current density normalized to the surface area of NiCu bimetallic catalysts. The grey dash line is drawn to guide the readers. The error bars represent at least three independent measurements.

We normalized the current density to the ECSA of NPs (derived in the earlier section) and plotted the ECSA-normalized current density against the iR-corrected potential, generating the Tafel plots of specific activity. As shown in Figure 3a, the HER Tafel plots of these NiCu/C catalysts are located across a potential window of ~300 mV, indicating the intrinsic activity difference is ~3 orders of magnitude. Of notable interest is that the intrinsic HER activity of Ni_2Cu_1/C approaches that of state-of-the-art Pt/C (Pt on carbon black, 20 wt%, Alfa Aesar), with an overpotential gap of ~100 mV. The HER activity was also tested in 1 M KOH, which gives the same performance as that in 0.1 M KOH (Figure S19). This observation rules out the presence of local acid-like environment at nanostructured catalysts in highly alkaline electrolyte.[54]

To examine the effect of surface composition on HER performance, the intrinsic activity, which is defined as the potential at a given specific current density of 1000 $\mu A/cm^2_{NPs}$, is plotted as a function of the surface Ni coverage. As shown in Figure 3b, their relationship forms a volcano-shaped trend, where the summit of HER activity is located at a surface Ni coverage of ~75% (Ni_2Cu_1/C). Too small or too large Ni content results in a lower HER activity than the intermediate Ni fraction. Such trend indicates that combining Ni with Cu can greatly enhance the HER activity; but further increasing the amount of Cu slows down the HER rate, even leading to an activity lower than pure Ni (i.e. Ni/C). Interestingly, this trend is consistent with a previous report, where HER activity at NiAg bulk alloys with various surface Ni content is maximized at $Ni_{0.75}Ag_{0.25}$ (a surface Ni coverage of 75%).[34] Caution that the validity of this established relationship between activity and surface composition (i.e. Ni coverage) depends on the stability of surface composition during HER measurement. If the surface composition keeps changing during HER measurement, it not only invalidates the relationship of activity vs. Ni coverage, but also the correlation between activity and surface-composition-dependent electronic structure (will be discussed later). To exclude this possibility, the surface composition was examined by CV after HER measurement, and results (Figure S20) show that CV before and after HER measurement almost overlap, indicating that the Ni:Cu ratio keeps unchanged during the HER measurement. To sum up, this section proves the HER activity at NiCu bimetallic catalysts is firmly correlated with surface Ni coverage, and next we dig for the underlying reason why activity forms such a volcano-shaped relationship with surface Ni coverage.

The position of d band center at NiCu bimetallic catalysts

The position of d band center relative to Fermi level, which is a measure of the strength of the metal-adsorbate interaction (i.e. hydrogen binding energy),[18-20] is postulated as the key descriptor for the varied alkaline HER activities at NiCu/C catalysts. The d band center theory for activity prediction is explained as follows.[19] The variation in the hydrogen-metal bond depends, to a large extent, on the strength of the coupling between the hydrogen s states and the metal d states. This coupling forms bonding and antibonding states as illustrated in Figure S21. The bonding states are filled, and the filling of the antibonding states, which governs the strength of hydrogen binding, varies from surface to surface. In a metallic environment, the filling depends on the position of the states relative to the Fermi level. An upward shift of the d states relative to the Fermi level results in an upward shift of the antibonding states, leading to less filling and thus a stronger bond; and vice versa. It is possible that the d band-governed H adsorption strength may not explain the alkaline HER, because the lack of protons in alkaline electrolyte necessitates water dissociation, where OH binding strength determines the rate for converting water to available protons and thus the overall HER rate.[14-16, 55] Nevertheless, hydrogen binding energy can act as the sole descriptor, as demonstrated by, for example, the fact that hydrogen binding energy has successfully explained the HER at monometallic catalysts across

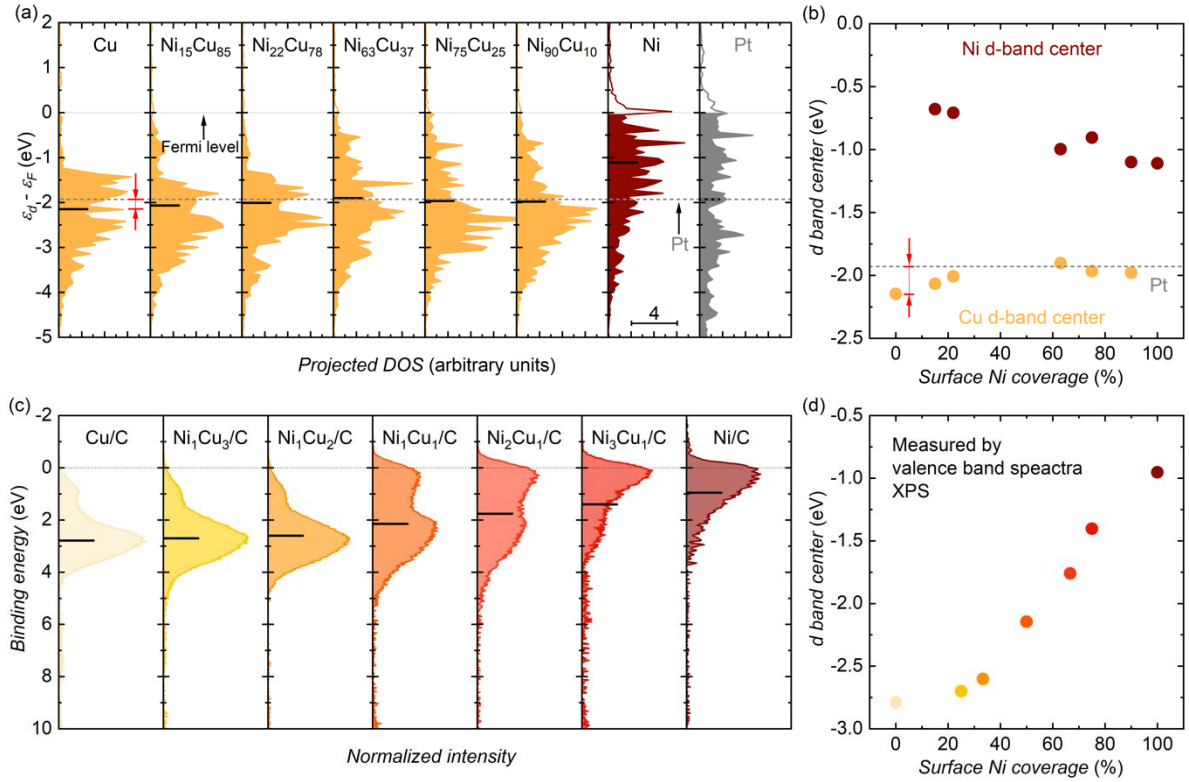

Figure 4. (a) The projected d band density of states (DOS) for NiCu model surfaces with various fractions of Ni atoms calculated by density functional theory (DFT). ε_d - ε_f is the energy of d band spectra (ε_d) relative to Fermi level (ε_f). The position of d band center is indicated by the short black horizontal bar. The grey solid line indicates the Fermi level. The grey dash line indicates the d band center of Pt. (b) The d band center of various NiCu surfaces calculated by DFT. Yellow points are d band centers of Cu, red are Ni; and the grey dash line is d band center of Pt. The distance relative to d band center of Pt is indicated by the red arrow in panel (a) and (b). (c) Normalized valence band spectra (VBS) of various NiCu/C catalysts measured by X-ray photoelectron spectroscopy (XPS). The valence band spectra are corrected for background with a Shirley-type baseline. The d band center position (which is the weight center of VBS, derived after subtraction of the Shirley-type background and integration) is marked by the horizontal black bar in panel (c) and plotted against surface Ni coverage in panel (d).

various pH values;[9, 12-13, 17] and a recent review that summarizes a set of evidences that prove OH binding plays a minor role in alkaline HER (which will be discussed explicitly in the next section).[17] This descriptor role of hydrogen binding energy in pH-dependent HER gives a hint that alkaline HER might be described by d band center, which, in the conventional point of view, is a rational reflection of hydrogen binding energy. In the following, the position of d band center of NiCu/C catalyst is quantified via two methods: DFT calculation; and experimental estimation by valence band spectra of XPS measurement.

Our DFT calculation results show that the d band center of NiCu bimetallic surface varies with Ni percentage (as a result of the ligand effect),[20] and we propose and rationalize a simplified model where d band center at Cu atom dominates HER at each NiCu surface. To represent each NiCu/C catalyst, we built a NiCu alloy model, where the Ni:Cu ratio is consistent with the surface composition revealed by CV measurement in an earlier section (see the detailed Ni fraction in Figure 4a or S22). Since DFT cannot give the cumulated d band of Ni and Cu, the calculated d band density of states (DOS) of both Ni and Cu atom at NiCu are shown in Figure S23. It is observed that by combining Cu with Ni, the position of d band at either Cu site or Ni site varies with the Ni content, which is due to the ligand effect.[20] The position of d band center was then quantified and shown in Figure 4a and 4b, along with that of Pt as an important reference. The reliability of our DFT calculation is confirmed by the fact that our quantified d band centers of pure Cu, Ni and Pt agree well with those in a landmark work.[19] Since Pt is an extremely active HER catalyst,[56-57] its d band center position, i.e. -1.929 eV with respect to the Fermi level, is usually considered to be optimal for having a most favorable hydrogen binding energy. Thus, the comparison with the d band center of Pt is a rational methodology for predicting the activity of a particular metal catalyst. With Pt as the reference, we can see the d band center of Ni atom at each NiCu surface locates at a more high-lying position than Pt, implying that the H adsorption at Ni site is too strong (Figure 4b and S23). In contrast, with various Ni content, the d band center of Cu atom at each NiCu surface shifts around (keeps close to) that of Pt, indicating that Cu site of NiCu surface has a d band center position close to the optimal value (i.e. that of Pt). This observation signifies that, if simplifying the NiCu surface by taking Ni and Cu separately, the Ni site at NiCu plays a minor role in HER (due to its too high-lying d band), and Cu is a more favorable catalytic site that dominates the HER activity. Therefore, to describe the various HER activity at NiCu surface, we propose a theoretical model, where the

HER at NiCu surface is simplified by taking Cu as the active site.

The d band center positions of various NiCu/C catalysts are experimentally estimated by valence band spectra (VBS) of XPS measurement. Different from DFT-derived results, the VBS-measured d band center is the cumulated states of Ni and Cu, which cannot separate the electronic structure at Ni sites from that at Cu sites. After background-correction with a Shirley-type baseline,[58-59] the valence band spectra are shown in Figure 4c. As expected, from Cu/C to Ni/C (with an increasing Ni fraction), the d band spectrum gradually shifts upwards. The d band center is further quantified by estimating the weight center of VBS,[58-59] and the results are shown in Figure 4d. Combining Ni with Cu gives an intermediate d band center position between pure Ni and Cu; and the d band center can be finely tuned by varying the Ni fraction. Despite the oxygen adsorption is inevitable at Ni and Cu surface,[34, 45] the O adsorption interference in d band measurement is considered to be minor, because of these two evidences: our measured d band centers at Ni and Cu are consistent with the values measured by VBS-XPS at bulk Ni and Cu metals,[58] where the surface O adsorption is minimized (O is even invisible at XPS spectra); and it is a rational observation that increasing the Ni fraction gradually shifts the d band center towards to that of pure Ni. Since d band center is a parameter that cumulatively includes the influence from various surface structures such as strain, facet, alloying, steps, discussing the role of d band center excludes the need for considering the effect of these surface structures on HER (more detailed discussion in SI).[20, 60] In the next section, we attempt to study the relationship between HER activity and d band center position, which includes the DFT-derived d band center of Cu at NiCu surface and the XPS-measured cumulated d band center.

Correlation between HER activity and d band at NiCu bimetallic catalysts

The d band center is identified as the governing factor of HER activity at various NiCu/C catalysts. As mentioned above, the position of d band center relative to Pt can act as an indicator of the HER activity. Either it is the case that the d band sits higher or lower than Pt yields a sluggish HER rate. The HER activity is optimized in the case that the d band center location of a particular metal catalyst is close to that of Pt. Therefore, to represent the HER activity, we extract the distance between the d band center of Cu (which is rationalized as the active site in the earlier discussion) at NiCu surface and that of Pt. This distance of each NiCu bimetallic surface relative to Pt is plotted against the surface Ni coverage (as shown in Figure S24). The HER activity, which is reflected by the as-extracted distance, forms a volcano-shaped relationship with surface Ni coverage, and the summit is located at ~65%. This trend is consistent with the volcano-type correlation between the experimentally measured HER activity and ECSA-determined surface Ni coverage. The climax of the experimental-derived volcano profile is ~75%, which is almost the same as the activity predicted from our proposed d band model. Such agreement validates our simplified model, where a surface Cu atom is taken as the active site, and thus the d band center at Cu appears to be an appropriate governing factor of HER activity at our NiCu bimetallic catalysts.

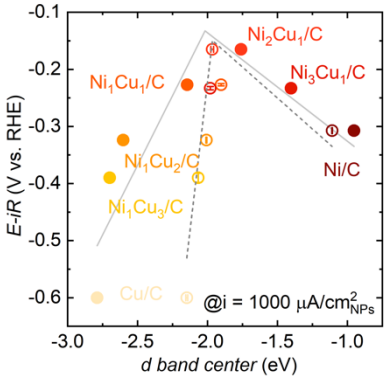

Figure 5. HER specific activity of various NiCu/C catalysts as a function of d band center. The d band center is estimated by two method: the open circle represents the d band center calculated by density function theory (DFT); and the solid circles indicate the d band center measured by X-ray photoelectron spectroscopy (XPS). The specific activity is defined as the potential at 1000 $\mu A/cm^2_{NPs}$, which is the current density normalized to the surface area of NiCu bimetallic catalysts. The grey lines are drawn to guide the readers. The error bars represent at least three independent measurements.

To further confirm the dominant role of d band center, we establish another two trends: one is the relationship between the HER activity at each NiCu/C catalyst and its d band center at Cu (given by DFT); the other is the correlation between HER activity and experimentally measured d band center. As shown in Figure 5, the HER activity (the specific activity normalized to the surface area of NiCu bimetallic catalysts) forms a striking volcano shape with either DFT-derived or the XPS-measured d band center, which illustrates very well the Sabatier principle,[32] and proves that d band center position is the dominant descriptor for alkaline HER at NiCu bimetallic catalysts. The d band center theory explains the volcano-shaped trend of HER activity vs. Ni coverage (Figure 3b). Recall Figure 3b demonstrates that Ni coverage can describe the activity trend: neither too high nor too low Ni coverage cannot give a high HER activity; an intermediate Ni coverage optimizes the activity. This is because the d band center and Ni coverage is strongly related: the variation of d band center originates from the ligand effect induced by various Ni coverages; thus d band center is the underlying reason why HER activity correlates with Ni coverage via a volcano trend. It is noticed that the established volcano trend (Figure 5) has some deviations: some data points are not perfectly located on the predicted position. For example, compared with Ni, Cu has a d band center closer to Pt, implying that Cu should have a higher HER activity than Ni; however, HER activity at Cu is much lower than Ni, which is consistent with the previous measurements.[2, 9] Here we attempt to rationalize such deviations by the following discussion. First, the established volcano-shaped relationship is usually asymmetrical. It is shown that Cu is located at the left branch of the volcano, and Ni is at the right (Figure 5). Considering this, a d band center closer to Pt does not necessarily give a higher HER activity,

unless the volcano trend is a symmetrical volcano shape. In fact, the activity-descriptor correlation is usually not a symmetrical volcano shape, for example, H adsorption strength in HER,[9] O-2p in oxygen evolution reaction (OER),[61] O adsorption in oxygen reduction reaction (ORR),[62] d band in ORR,[21] e_g in OER/ORR.[1, 4] Second, the deviations are understandable and in some cases, even inevitable. Similar deviations are also present in the volcano trends established in the landmark descriptor studies,[1-2, 9, 62] indicating that as long as the activity forms a clear volcano-shaped relationship with the descriptor, the deviation does not affect the successful identification of a descriptor. The deviation is even inevitable, because the established descriptors in literature, including our d band center in this work, are dominant descriptors, which usually fail to include some minor influential factor. For example, quantifying the d band center by calculating the weight center of d band spectra may neglect the effect of d band shape on reactivity.[63] Possiblly due to the unnoticed minor factors, the linear relationship between H binding energy and d band center is not a perfect straight line (deviations exist, see ref [30]); and thus the trend of activity versus d band center (an indicator of H binding energy) unavoidably presents deviations.

The descriptor role of d band center in alkaline HER also proves our earlier postulation that the alkaline HER at NiCu bimetallic catalysts does not rely on the availability of protons, which has been widely reported in literature. In particular, a recent review[17] has summarized a set of evidences to prove the minor role of water dissociation in alkaline HER, and here we reference several key proofs to rationalize our postulation. The experimental design that fixes H adsorption and meanwhile varies OH binding energy allows us to identify the role of OH binding. Following this logic, the comparison between PtNi and acid-leached PtNi, which have the same H adsorption strength but different OH binding energies, shows that they have the same alkaline HER/HOR activity, and thus indicating OH binding does not affect HER.[64] It is usually believed that the reactant for HER in acid is H^+ (or H_3O^+); and that for alkaline HER is H_2O, which needs to be dissociated to produce protons. Evidences indicate that, however, H_2O can act as the proton donor/acceptor in acid, as water dissociation step is always at fast equilibrium across various pH values.[17, 57, 65] Thus the reactants for HER in acid and base are the same. The catalyst surface takes either protons or water molecules as the reactants for HER in alkaline electrolyte; these two reactants share the equal chances to be catalyzed. Durst et al.[57] argue that, under the assumption water dissociation is an indispensable step, a combination of Pt (known to be active for hydrogen recombination) with more oxophilic metals (e.g. Ir) would enhance the interaction with H_2O/OH^- to yield higher alkaline HER activities.[55] Thus, if OH binding plays a major role, increasing the Ni coverage (Ni is more oxophilic than Pt and the existence of surface Ni can significantly promote the OH adsorption)[64] of our NiCu bimetallic catalysts would have led to a monotonic increase of alkaline HER activity. However, a volcano-type trend is observed (Figure 5), indicating OH adsorption is not a major role in our study. We understand OH binding could be another descriptor of the catalytic activity for alkaline HER (as reported by numerous publications).[14-16, 55, 66] The role of OH adsorption in alkaline HER, however, is currently still under debate; and the findings presented in this paper suggest that the d band-governed hydrogen binding energy appears to be an appropriate descriptor for alkaline HER at bimetallic NiCu catalysts. We hope more evidences will be presented in the future to clear the debate about the exact role of OH adsorption in alkaline HER.

DFT-calculated hydrogen binding energy at NiCu bimetallic catalysts

Since d band theory relates to the adsorption energy of adsorbates, this section studies hydrogen binding energy to further rationalize (and supplement) the d band theory for explaining HER activity at various NiCu/C catalysts. We understand that our proposed DFT-derived d band model (in the earlier section) may be too simple, as it simplifies the catalyst surface by taking Ni and Cu separately, and fails to consider the hollow site adsorption, which usually takes

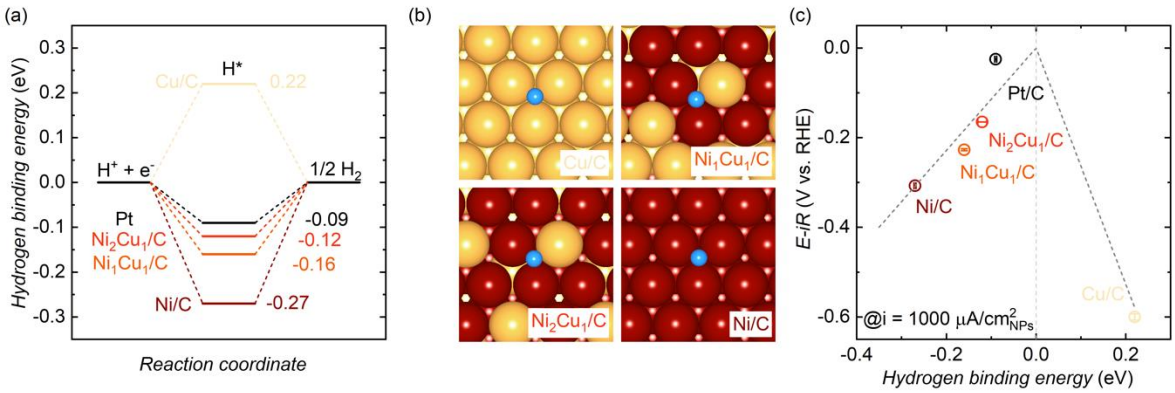

Figure 6. (a) The hydrogen binding energy at Cu, $Ni_{63}Cu_{37}$, $Ni_{75}Cu_{25}$, Ni and Pt model surfaces, which represent the catalyst Cu/C, Ni_1Cu_1/C, Ni_2Cu_1/C and Ni/C, respectively. (b) The selected illustrations of the calculated surface sites for hydrogen (H) adsorption. The yellow spheres are Cu, red spheres are Ni and blue spheres are H. (c) The hydrogen evolution reaction specific activity as a function of the calculated hydrogen binding energy at Cu/C, Ni_1Cu_1/C, Ni_2Cu_1/C and Ni/C, which are based on the model of Cu, $Ni_{63}Cu_{37}$, $Ni_{75}Cu_{25}$ and Ni, respectively. The specific activity is defined as the potential at 1000 $\mu A/cm^2_{NPs}$, which is the current density normalized to the surface area of NiCu bimetallic catalysts.

place in "actual" situation. Here, with supplementary evidence of hydrogen binding energy, we demonstrate the rationale of this simplified model, which could reasonably reflect the hollow site adsorption. The top two catalysts in our NiCu series were selected to calculate the hydrogen binding energy (Table S1). The hydrogen binding energies are shown in Figure 6a, and the corresponding adsorption sites are visualized in Figure 6b. As shown in Figure 6a, the hydrogen binding energies of the hollow site at Ni_1Cu_1/C and Ni_2Cu_1/C are -0.16 eV and -0.12 eV, respectively, which are close to the optimum value (i.e. 0 eV) and the benchmark value of Pt (i.e. -0.09 eV). This evidence demonstrates that the combination of Ni and Cu indeed generates some highly active NiCu structures and explains the high activities of these two NiCu/C catalysts. By plotting HER activity against the hydrogen binding energy at these exemplary catalysts (Figure 6c), it elucidates the origin of the superior activity of Ni_2Cu_1/C to Ni_1Cu_1/C: the hydrogen binding energy at Ni_2Cu_1/C is closer to the optimum value. This is consistent with our earlier d band center observation (Figure 5), where the d band center at Ni_2Cu_1/C is more optimized than Ni_1Cu_1/C. The agreement between the activity trend versus hydrogen binding energy (i.e. Figure 6c) and that as a function of d band center validates the descriptor role of d band center (i.e. Figure 5), despite the simplicity of our proposed DFT-derived d band theory.

Conclusions

In summary, we aim to investigate the role of d band in alkaline HER with NiCu bimetallic surface as the model catalyst. The surface compositional ratio of Ni to Cu is varied to control the ligand effect, and thus to tune the position of d band center, which is quantified by DFT calculation and XPS measurement. The intrinsic HER activity of NiCu bimetallic catalyst exhibits a volcano-shaped dependence on the d band position, which indicates that the d band center can be used as a descriptor for alkaline HER. The descriptor role of d band center is further supported by the evidence that the combination of Ni and Cu produces a variety of adsorption sites, which possess near-optimal hydrogen binding energy. Our finding reinforces the guiding role of d band theory in searching for metal electrocatalysts, and may provide some inspiring insights for understanding the alkaline HER mechanism.

ASSOCIATED CONTENT

Supporting Information. The Supporting Information is available free of charge via the Internet at http://pubs.acs.org. Experimental details, XRD, TEM, CVs, XPS, DFT calculations, etc. (PDF)

AUTHOR INFORMATION

Corresponding Author

*xuzc@ntu.edu.sg

Author Contributions

ΔThese authors contributed equally.

Notes

The authors declare no competing financial interest.

ACKNOWLEDGMENT

This work was supported by Singapore Ministry of Education Tier 2 Grant (MOE2017-T2-1-009) and the Campus for Research Excellence and Technological Enterprise (CREATE), through the Singapore Berkeley Research Initiative for Sustainable Energy (SinBeRISE), The Cambridge Center for Carbon Reduction in Chemical Technology (C4T), and eCO2EP programmes. The authors acknowledge the Facility for Analysis, Characterization, Testing and Simulation, Nanyang Technological University, Singapore, for use of their electron microscopy/X-ray facilities.

REFERENCES

(1) Hong, W. T.; Risch, M.; Stoerzinger, K. A.; Grimaud, A.; Suntivich, J.; Shao-Horn, Y., Toward the rational design of non-precious transition metal oxides for oxygen electrocatalysis. *Energy Environ. Sci.* **2015,** *8*, 1404-1427.

(2) Seh, Z. W.; Kibsgaard, J.; Dickens, C. F.; Chorkendorff, I.; Nørskov, J. K.; Jaramillo, T. F., Combining theory and experiment in electrocatalysis: Insights into materials design. *Science* **2017,** *355*, eaad4998-eaad5009.

(3) Wu, T.; Sun, S.; Song, J.; Xi, S.; Du, Y.; Chen, B.; Sasangka, W. A.; Liao, H.; Gan, C. L.; Scherer, G. G.; Zeng, L.; Wang, H.; Li, H.; Grimaud, A.; Xu, Z. J., Iron-facilitated dynamic active-site generation on spinel CoAl2O4 with self-termination of surface reconstruction for water oxidation. *Nat. Catal.* **2019,** *2*, 763-772.

(4) Wei, C.; Feng, Z.; Scherer, G. G.; Barber, J.; Shao-Horn, Y.; Xu, Z. J., Cations in Octahedral Sites: A Descriptor for Oxygen Electrocatalysis on Transition-Metal Spinels. *Adv. Mater.* **2017,** *29*, 1606800.

(5) Montoya, J. H.; Seitz, L. C.; Chakthranont, P.; Vojvodic, A.; Jaramillo, T. F.; Nørskov, J. K., Materials for solar fuels and chemicals. *Nat. Mater.* **2016,** *16*, 70-81.

(6) Wei, C.; Rao, R. R.; Peng, J.; Huang, B.; Stephens, I. E. L.; Risch, M.; Xu, Z. J.; Shao-Horn, Y., Recommended Practices and Benchmark Activity for Hydrogen and Oxygen Electrocatalysis in Water Splitting and Fuel Cells. *Adv. Mater.* **2019,** *31*, 1806296.

(7) Ledezma-Yanez, I.; Wallace, W. D. Z.; Sebastián-Pascual, P.; Climent, V.; Feliu, J. M.; Koper, M. T. M., Interfacial water reorganization as a pH-dependent descriptor of the hydrogen evolution rate on platinum electrodes. *Nat. Energy* **2017,** *2*, 17031-17037.

(8) Kibsgaard, J.; Tsai, C.; Chan, K.; Benck, J. D.; Norskov, J. K.; Abild-Pedersen, F.; Jaramillo, T. F., Designing an improved transition metal phosphide catalyst for hydrogen evolution using experimental and theoretical trends. *Energy Environ. Sci.* **2015,** *8*, 3022-3029.

(9) Sheng, W.; Myint, M.; Chen, J. G.; Yan, Y., Correlating the hydrogen evolution reaction activity in alkaline electrolytes with the hydrogen binding energy on monometallic surfaces. *Energy Environ. Sci.* **2013,** *6*, 1509-1512.

(10) Liu, J.; Zhu, D.; Ling, T.; Vasileff, A.; Qiao, S.-Z., S-NiFe2O4 ultrasmall nanoparticle built nanosheets for efficient water splitting in alkaline and neutral pH. *Nano Energy* **2017,** *40*, 264-273.

(11) Ling, T.; Zhang, T.; Ge, B.; Han, L.; Zheng, L.; Lin, F.; Xu, Z.; Hu, W.-B.; Du, X.-W.; Davey, K.; Qiao, S.-Z., Well-Dispersed Nickel- and Zinc-Tailored Electronic Structure of a Transition Metal Oxide for Highly Active Alkaline Hydrogen Evolution Reaction. *Adv. Mater.* **2019,** *31*, 1807771.

(12) Sheng, W.; Zhuang, Z.; Gao, M.; Zheng, J.; Chen, J. G.; Yan, Y., Correlating hydrogen oxidation and evolution activity on platinum at different pH with measured hydrogen binding energy. *Nat. Commun.* **2015,** *6*, 5848-5853.

(13) Zheng, J.; Sheng, W.; Zhuang, Z.; Xu, B.; Yan, Y., Universal dependence of hydrogen oxidation and evolution reaction activity of platinum-group metals on pH and hydrogen binding energy. *Sci. Adv.* **2016,** *2*, e1501602-e1501609.

(14) Subbaraman, R.; Tripkovic, D.; Strmcnik, D.; Chang, K.-C.; Uchimura, M.; Paulikas, A. P.; Stamenkovic, V.; Markovic, N. M., Enhancing Hydrogen Evolution Activity in Water Splitting by Tailoring Li+-Ni(OH)2-Pt Interfaces. *Science* **2011,** *334*, 1256-1260.
(15) Danilovic, N.; Subbaraman, R.; Strmcnik, D.; Chang, K.-C.; Paulikas, A. P.; Stamenkovic, V. R.; Markovic, N. M., Enhancing the Alkaline Hydrogen Evolution Reaction Activity through the Bifunctionality of Ni(OH)2/Metal Catalysts. *Angew. Chem., Int. Ed.* **2012,** *51*, 12495-12498.
(16) Subbaraman, R.; Tripkovic, D.; Chang, K.-C.; Strmcnik, D.; Paulikas, A. P.; Hirunsit, P.; Chan, M.; Greeley, J.; Stamenkovic, V.; Markovic, N. M., Trends in activity for the water electrolyser reactions on 3d M(Ni,Co,Fe,Mn) hydr(oxy)oxide catalysts. *Nat. Mater.* **2012,** *11*, 550-557.
(17) Tian, X.; Zhao, P.; Sheng, W., Hydrogen Evolution and Oxidation: Mechanistic Studies and Material Advances. *Adv. Mater.* **2019,** *31*, 1808066.
(18) Hammer, B.; Norskov, J. K., Why gold is the noblest of all the metals. *Nature* **1995,** *376*, 238-240.
(19) Nørskov, J. K.; Studt, F.; Abild-Pedersen, F.; Bligaard, T., The Electronic Factor in Heterogeneous Catalysis. In *Fundamental Concepts in Heterogeneous Catalysis*, John Wiley & Sons, Inc: 2014; pp 114-137.
(20) Bligaard, T.; Nørskov, J. K., Ligand effects in heterogeneous catalysis and electrochemistry. *Electrochim. Acta* **2007,** *52*, 5512-5516.
(21) Stamenkovic, V.; Mun, B. S.; Mayrhofer, K. J. J.; Ross, P. N.; Markovic, N. M.; Rossmeisl, J.; Greeley, J.; Nørskov, J. K., Changing the Activity of Electrocatalysts for Oxygen Reduction by Tuning the Surface Electronic Structure. *Angew. Chem. Int. Ed.* **2006,** *118*, 2963-2967.
(22) Stamenkovic, V. R.; Mun, B. S.; Arenz, M.; Mayrhofer, K. J.; Lucas, C. A.; Wang, G.; Ross, P. N.; Markovic, N. M., Trends in electrocatalysis on extended and nanoscale Pt-bimetallic alloy surfaces. *Nat. Mater.* **2007,** *6*, 241-247.
(23) Strasser, P.; Koh, S.; Anniyev, T.; Greeley, J.; More, K.; Yu, C.; Liu, Z.; Kaya, S.; Nordlund, D.; Ogasawara, H.; Toney, M. F.; Nilsson, A., Lattice-strain control of the activity in dealloyed core–shell fuel cell catalysts. *Nat. Chem.* **2010,** *2*, 454-460.
(24) Lima, F. H. B.; Zhang, J.; Shao, M. H.; Sasaki, K.; Vukmirovic, M. B.; Ticianelli, E. A.; Adzic, R. R., Catalytic activity−d-band center correlation for the O2 reduction reaction on platinum in alkaline solutions. *J. Phys. Chem. C* **2006,** *111*, 404-410.
(25) Wu, Y.; Liu, X.; Han, D.; Song, X.; Shi, L.; Song, Y.; Niu, S.; Xie, Y.; Cai, J.; Wu, S.; Kang, J.; Zhou, J.; Chen, Z.; Zheng, X.; Xiao, X.; Wang, G., Electron density modulation of NiCo2S4 nanowires by nitrogen incorporation for highly efficient hydrogen evolution catalysis. *Nat. Commun.* **2018,** *9*, 1425-1433.
(26) Pan, Y.; Sun, K.; Lin, Y.; Cao, X.; Cheng, Y.; Liu, S.; Zeng, L.; Cheong, W.-C.; Zhao, D.; Wu, K.; Liu, Z.; Liu, Y.; Wang, D.; Peng, Q.; Chen, C.; Li, Y., Electronic structure and d-band center control engineering over M-doped CoP (M = Ni, Mn, Fe) hollow polyhedron frames for boosting hydrogen production. *Nano Energy* **2019,** *56*, 411-419.
(27) Chen, Z.; Song, Y.; Cai, J.; Zheng, X.; Han, D.; Wu, Y.; Zang, Y.; Niu, S.; Liu, Y.; Zhu, J.; Liu, X.; Wang, G., Tailoring the d-Band Centers Enables Co4N Nanosheets To Be Highly Active for Hydrogen Evolution Catalysis. *Angew. Chem., Int. Ed.* **2018,** *57*, 5076-5080.
(28) Shao, Q.; Wang, Y.; Yang, S.; Lu, K.; Zhang, Y.; Tang, C.; Song, J.; Feng, Y.; Xiong, L.; Peng, Y.; Li, Y.; Xin, H. L.; Huang, X., Stabilizing and Activating Metastable Nickel Nanocrystals for Highly Efficient Hydrogen Evolution Electrocatalysis. *ACS Nano* **2018,** *12*, 11625-11631.
(29) Gou, W.; Li, J.; Gao, W.; Xia, Z.; Zhang, S.; Ma, Y., Downshifted d-Band Center of Ru/MWCNTs by Turbostratic Carbon Nitride for Efficient and Robust Hydrogen Evolution in Alkali. *ChemCatChem* **2019,** *11*, 1970-1976.
(30) Jiao, Y.; Zheng, Y.; Jaroniec, M.; Qiao, S. Z., Design of electrocatalysts for oxygen- and hydrogen-involving energy conversion reactions. *Chem. Soc. Rev.* **2015,** *44*, 2060-2086.
(31) Yang, J.; Shao, Q.; Huang, B.; Sun, M.; Huang, X., pH-Universal Water Splitting Catalyst: Ru-Ni Nanosheet Assemblies. *iScience* **2019,** *11*, 492-504.
(32) Medford, A. J.; Vojvodic, A.; Hummelshøj, J. S.; Voss, J.; Abild-Pedersen, F.; Studt, F.; Bligaard, T.; Nilsson, A.; Nørskov, J. K., From the Sabatier principle to a predictive theory of transition-metal heterogeneous catalysis. *J. Catal.* **2015,** *328*, 36-42.
(33) Sheng, W.; Bivens, A. P.; Myint, M.; Zhuang, Z.; Forest, R. V.; Fang, Q.; Chen, J. G.; Yan, Y., Non-precious metal electrocatalysts with high activity for hydrogen oxidation reaction in alkaline electrolytes. *Energy Environ. Sci.* **2014,** *7*, 1719-1724.
(34) Tang, M. H.; Hahn, C.; Klobuchar, A. J.; Ng, J. W. D.; Wellendorff, J.; Bligaard, T.; Jaramillo, T. F., Nickel-silver alloy electrocatalysts for hydrogen evolution and oxidation in an alkaline electrolyte. *Phys. Chem. Chem. Phys.* **2014,** *16*, 19250-19257.
(35) Yin, J.; Fan, Q.; Li, Y.; Cheng, F.; Zhou, P.; Xi, P.; Sun, S., Ni–C–N Nanosheets as Catalyst for Hydrogen Evolution Reaction. *J. Am. Chem. Soc.* **2016,** *138*, 14546-14549.
(36) Lu, Q.; Hutchings, G. S.; Yu, W.; Zhou, Y.; Forest, R. V.; Tao, R.; Rosen, J.; Yonemoto, B. T.; Cao, Z.; Zheng, H.; Xiao, J. Q.; Jiao, F.; Chen, J. G., Highly porous non-precious bimetallic electrocatalysts for efficient hydrogen evolution. *Nat. Commun.* **2015,** *6*, 6567-6574.
(37) Wang, X.; Zhu, Y.; Vasileff, A.; Jiao, Y.; Chen, S.; Song, L.; Zheng, B.; Zheng, Y.; Qiao, S.-Z., Strain Effect in Bimetallic Electrocatalysts in the Hydrogen Evolution Reaction. *ACS Energy Letters* **2018,** *3*, 1198-1204.
(38) Conway, B. E.; Bai, L., Determination of the adsorption behaviour of 'overpotential-deposited' hydrogen-atom species in the cathodic hydrogen-evolution reaction by analysis of potential-relaxation transients. *J. Chem. Soc., Faraday Trans. 1* **1985,** *81*, 1841-1862.
(39) Perdew, J. P.; Burke, K.; Ernzerhof, M., Generalized Gradient Approximation Made Simple. *Phys. Rev. Lett.* **1996,** *77*, 3865-3868.
(40) Zhang, Y.; Yang, W., Comment on ``Generalized Gradient Approximation Made Simple''. *Phys. Rev. Lett.* **1998,** *80*, 890-890.
(41) Monkhorst, H. J.; Pack, J. D., Special points for Brillouin-zone integrations. *Phys. Rev. B* **1976,** *13*, 5188-5192.
(42) Nørskov, J. K.; Bligaard, T.; Logadottir, A.; Kitchin, J. R.; Chen, J. G.; Pandelov, S.; Stimming, U., Trends in the Exchange Current for Hydrogen Evolution. *J. Electrochem. Soc.* **2005,** *152*, J23-J26.
(43) Suntivich, J.; Xu, Z.; Carlton, C. E.; Kim, J.; Han, B.; Lee, S. W.; Bonnet, N.; Marzari, N.; Allard, L. F.; Gasteiger, H. A.; Hamad-Schifferli, K.; Shao-Horn, Y., Surface composition tuning of Au-Pt bimetallic nanoparticles for enhanced carbon monoxide and methanol electro-oxidation. *J. Am. Chem. Soc.* **2013,** *135*, 7985-7991.
(44) Lin, Z.; Li, J.; Li, L.; Yu, L.; Li, W.; Yang, G., Manipulating the hydrogen evolution pathway on composition-tunable CuNi nanoalloys. *J. Mater. Chem. A* **2017,** *5*, 773-781.
(45) Wang, M.; Wang, L.; Li, H.; Du, W.; Khan, M. U.; Zhao, S.; Ma, C.; Li, Z.; Zeng, J., Ratio-Controlled Synthesis of CuNi Octahedra and Nanocubes with Enhanced Catalytic Activity. *J. Am. Chem. Soc.* **2015,** *137*, 14027-14030.
(46) Li, D.; Wang, C.; Tripkovic, D.; Sun, S.; Markovic, N. M.; Stamenkovic, V. R., Surfactant Removal for Colloidal Nanoparticles from Solution Synthesis: The Effect on Catalytic Performance. *ACS Catal.* **2012,** *2*, 1358-1362.
(47) Wei, C.; Sun, S.; Mandler, D.; Wang, X.; Qiao, S. Z.; Xu, Z. J., Approaches for measuring the surface areas of metal oxide electrocatalysts for determining their intrinsic electrocatalytic activity. *Chem. Soc. Rev.* **2019,** *48*, 2518-2534.
(48) Zheng, J.; Zhou, S.; Gu, S.; Xu, B.; Yan, Y., Size-Dependent Hydrogen Oxidation and Evolution Activities on Supported Palladium Nanoparticles in Acid and Base. *J. Electrochem. Soc.* **2016,** *163*, F499-F506.

(49) Machado, S. A. S.; Avaca, L. A., The hydrogen evolution reaction on nickel surfaces stabilized by H-absorption. *Electrochim. Acta* **1994,** *39*, 1385-1391.
(50) Fletcher, S.; Barradas, R. G.; Porter, J. D., The Anodic Oxidation of Copper Amalgam and Polycrystalline Copper Electrodes in LiOH Solution. *J. Electrochem. Soc.* **1978,** *125*, 1960-1968.
(51) Zhou, Y.; Xi, S.; Wang, J.; Sun, S.; Wei, C.; Feng, Z.; Du, Y.; Xu, Z. J., Revealing the Dominant Chemistry for Oxygen Reduction Reaction on Small Oxide Nanoparticles. *ACS Catal.* **2018,** *8*, 673-677.
(52) Sheng, W.; Chen, S.; Vescovo, E.; Shao-Horn, Y., Size Influence on the Oxygen Reduction Reaction Activity and Instability of Supported Pt Nanoparticles. *J. Electrochem. Soc.* **2012,** *159*, B96-B103.
(53) Wei, C.; Xu, Z. J., The Comprehensive Understanding of 10 mA cm-2geo as an Evaluation Parameter for Electrochemical Water Splitting. *Small Methods* **2018**, 1800168.
(54) Wang, X.; Xu, C.; Jaroniec, M.; Zheng, Y.; Qiao, S.-Z., Anomalous hydrogen evolution behavior in high-pH environment induced by locally generated hydronium ions. *Nat. Commun.* **2019,** *10*, 4876-4883.
(55) Strmcnik, D.; Uchimura, M.; Wang, C.; Subbaraman, R.; Danilovic, N.; van der Vliet, D.; Paulikas, A. P.; Stamenkovic, V. R.; Markovic, N. M., Improving the hydrogen oxidation reaction rate by promotion of hydroxyl adsorption. *Nat. Chem.* **2013,** *5*, 300-306.
(56) Sheng, W.; Gasteiger, H. A.; Shao-Horn, Y., Hydrogen oxidation and evolution reaction kinetics on platinum: acid vs alkaline electrolytes. *J. Electrochem. Soc.* **2010,** *157*, B1529-B1536.
(57) Durst, J.; Siebel, A.; Simon, C.; Hasche, F.; Herranz, J.; Gasteiger, H. A., New insights into the electrochemical hydrogen oxidation and evolution reaction mechanism. *Energy Environ. Sci.* **2014,** *7*, 2255-2260.
(58) Hofmann, T.; Yu, T. H.; Folse, M.; Weinhardt, L.; Bär, M.; Zhang, Y.; Merinov, B. V.; Myers, D. J.; Goddard, W. A.; Heske, C., Using Photoelectron Spectroscopy and Quantum Mechanics to Determine d-Band Energies of Metals for Catalytic Applications. *J. Phys. Chem. C* **2012,** *116*, 24016-24026.
(59) Mun, B. S.; Watanabe, M.; Rossi, M.; Stamenkovic, V.; Markovic, N. M.; Jr., P. N. R., A study of electronic structures of Pt3M (M=Ti,V,Cr,Fe,Co,Ni) polycrystalline alloys with valence-band photoemission spectroscopy. *J. Chem. Phys.* **2005,** *123*, 204717-204720.
(60) Abild-Pedersen, F.; Greeley, J.; Nørskov, J. K., Understanding the Effect of Steps, Strain, Poisons, and Alloying: Methane Activation on Ni Surfaces. *Catal. Lett.* **2005,** *105*, 9-13.
(61) Grimaud, A.; May, K. J.; Carlton, C. E.; Lee, Y. L.; Risch, M.; Hong, W. T.; Zhou, J.; Shao-Horn, Y., Double perovskites as a family of highly active catalysts for oxygen evolution in alkaline solution. *Nat. Commun.* **2013,** *4*, 2439-2445.
(62) Nørskov, J. K.; Rossmeisl, J.; Logadottir, A.; Lindqvist, L.; Kitchin, J. R.; Bligaard, T.; Jónsson, H., Origin of the Overpotential for Oxygen Reduction at a Fuel-Cell Cathode. *J. Phys. Chem. B* **2004,** *108*, 17886-17892.
(63) Xin, H.; Vojvodic, A.; Voss, J.; Nørskov, J. K.; Abild-Pedersen, F., Effects of d-band shape on the surface reactivity of transition-metal alloys. *Phys. Rev. B* **2014,** *89*, 115114-115118.
(64) Lu, S.; Zhuang, Z., Investigating the Influences of the Adsorbed Species on Catalytic Activity for Hydrogen Oxidation Reaction in Alkaline Electrolyte. *J. Am. Chem. Soc.* **2017,** *139*, 5156-5163.
(65) Rossmeisl, J.; Chan, K.; Skúlason, E.; Björketun, M. E.; Tripkovic, V., On the pH dependence of electrochemical proton transfer barriers. *Catal. Today* **2016,** *262*, 36-40.
(66) Zheng, Y.; Jiao, Y.; Vasileff, A.; Qiao, S.-Z., The Hydrogen Evolution Reaction in Alkaline Solution: From Theory, Single Crystal Models, to Practical Electrocatalysts. *Angew. Chem., Int. Ed.* **2018,** *57*, 7568-7579.

Insert Table of Contents artwork here

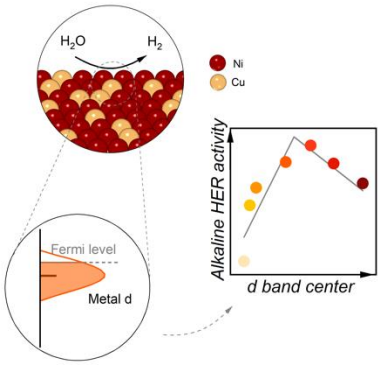

Supporting information

Surface Composition Dependent Ligand Effect in Tuning the Activity of Nickel-copper Bimetallic Electrocatalysts towards Hydrogen Evolution in Alkaline

Chao Wei,[†,└,Δ] Yuanmiao Sun,[†,Δ] Günther G. Scherer,[‡,§] Adrian C. Fisher,[‖] Matthew Sherburne,[▽] Joel W. Ager,[▽] Zhichuan J. Xu*[,†,└,⊥]

[†]School of Materials Science and Engineering, Nanyang Technological University, 50 Nanyang Avenue, 639798, Singapore;
[‡]Department for Management of Science and Technology Development, Ton Duc Thang University, Ho Chi Minh City, Vietnam;
[§]Faculty of Applied Sciences, Ton Duc Thang University, Ho Chi Minh City, Vietnam;
[‖]Department of Chemical Engineering, University of Cambridge, Cambridge CB2 3RA, UK;
[▽]Department of Materials Science and Engineering, University of California at Berkeley, Berkeley, California 94720, USA
[└]Solar Fuels Laboratory, Nanyang Technological University, 50 Nanyang Avenue, 639798, Singapore;
[⊥]Energy Research Institute @ Nanyang Technological University, 50 Nanyang Avenue, 639798, Singapore

[Δ]C. Wei and Y. Sun contributed equally

*Email: xuzc@ntu.edu.sg

Methods

Synthesis of NiCu nanoparticles (NPs). The NiCu NPs with various compositions were synthesized by reducing $Ni(acac)_2$ and $Cu(acac)_2$ in oleylamine. In a typical synthesis of Ni_1Cu_1, 0.5 mmol $Ni(acac)_2$, 0.5 mmol $Cu(acac)_2$, 10 ml oleylamine and 0.8 ml oleic acid were mixed at room temperature (25 °C). The solution was then kept at 120 °C under an Ar blanket for 30 min to remove the moisture. Then the solution was heated to 220 °C at a heating rate of 2 °C/min. The reaction was maintained at 220 °C for 1 hr and then naturally cooled down to room temperature. As-prepared Ni_1Cu_1 NPs were collected and washed by adding ~100 ml ethanol and following centrifugation. The composition was varied by changing the precursor ratio between $Ni(acac)_2$ and $Cu(acac)_2$; and the total amount of Ni and Cu precursor was kept at 1 mmol. NiCu NPs can be dispersed well in nonpolar solvents such as hexane and toluene.

Carbon loading. A suspension of Vulcan XC-72 (Premetek, USA) was prepared by sonicating ~320 mg of Vulcan in 600 ml hexane in an ice bath for 5 hours. Afterward, a suspension of as-prepared NiCu NPs in hexane was added into the Vulcan suspension and the mixture was further sonicated for 2 additional hours. The catalyst powders were collected by purging Ar (evaporating hexane) at room temperature and dried in vacuum oven for 24 hr. The mass loading of NiCu NPs at NiCu/C catalysts was controlled at 20 w%, which was confirmed by Inductively Coupled Plasma (ICP). The exceptional case is Ni/C, where the ICP measurement gave a Ni loading of 5 w%.

Heat treatment for surfactant removal. NiCu/C catalysts were placed in a tube furnace, and purged with dry air at a flow rate of 100 ml/min. The NiCu/C catalysts were heated up to 250 °C with a heating rate of 5 °C/min under air and maintained at this temperature for 30 min. After naturally cooling down to the room temperature, the air atmosphere was switched to a mixture of H_2/Ar (5% H_2) and the gas flow rate was kept at 100 ml/min. The temperature was further increased up to 200 °C with a heating rate of 5 °C/min and maintained for 1 hr. Subsequently, the tube furnace naturally cooled down to room temperature.

Physical characterization. The TEM study was carried out on a JEOL 2010 transmission electron microscope at 200 kV. The samples were prepared by dropping NPs suspension (in hexane) onto Cu TEM grids with amorphous carbon film. The X-ray diffraction pattern was collected on a PANalytical X'pert Pro with Cu Kα radiation (λ =1.5418 Å). The XRD samples were prepared by dropping highly concentrated NPs suspension onto glass slides. The composition of NPs was determined by ICP. For X-ray photoelectron spectroscopy (XPS) experiments a PHI5700 spectrometer, made by Physical Electronics, was employed. To measure the d band, XPS technique was chosen by referencing an article, which recommends XPS as a more favorable choice than UPS.[1] Monochromatized X-ray Al Kα radiation of energy equal to 1486 eV was used. XPS valence band spectra were collected with 0.8 eV resolution due to the low cross section of VB electrons to Al Kα photons.

Preparation of the working electrodes. Working electrodes were fabricated by drop-casting catalysts onto rotating disk electrode (RDE) with a modified ink recipe as described previously.[2] The as-prepared NiCu/C catalysts were dispersed in a mixture of solvents containing water, isopropanol and Nafion® perfluorinated resin solution (5 wt% in water) (v/v/v = 4/1/0.04). After sonicating for 1 hr in an ice bath, 15 μL of this ink was then dropped onto the glassy carbon RDE electrode (5 mm diameter) and dried at room temperature, yielding a metal mass loading of 2 μg_{metal} (10.2 $\mu g_{metal}/cm^2_{disk}$).The preparation of commercial Pt/C (Alfa Aesar, 20 w%) electrode follows the same recipe as NiCu/C catalysts.

Measurement of hydrogen evolution reaction (HER) activity. HER tests were conducted in a three-electrode cell, where the working electrode compartment and counter electrode compartment were separated by AMI-7001 anion exchange membrane to avoid Pt contamination from Pt counter electrode. The membrane was immersed in 0.1 M KOH solution overnight before the test.

Electrochemical data was recorded by a BioLogic SP-150 potentiostat at room temperature (25 °C). A Pt foil served as counter electrode and a mercury-mercury oxide (Hg/HgO, filled with 0.1 M KOH solution) was used as reference electrode. The HER performance was assessed by the cyclic voltammetry (CV) at 10 mV/s with a rotation speed of 1600 rpm in H_2-saturated 0.1 M KOH (prepared by Sigma-Aldrich potassium hydroxide, assay 99.99%).

The applied potentials were converted to the RHE scale via reference electrode calibration in H_2-saturated 0.1 M KOH. The potentials were further iR-corrected by the equation: $E = E_{applied} - iR$, where R (the uncompensated resistance) was measured by electrochemical impedance spectroscopy (EIS). Our cell setup (from PINE Instruments) gives a R value of ~45 Ω. One of the alternative methods is to dynamically compensate for the iR in modern potentiostats.[3] However, this application is not advisable because the circuit consisting of the potentiostat and the electrochemical cell could drift into the resonance condition by subtle changes of the electrolyte or the catalyst, thereby compromising the measurements.[3] Other methods such as current interrupt, and high frequency resistance can also measure the R for iR-correction.[4] However, a systematic study proves that either the R measured by current interrupt technique or high frequency resistance gives a larger value than the R by EIS,[4] which indicates that EIS has a minimal possibility to overcorrect iR. The iR may be overcorrected in the case that R is measured at a high overpotential, where gas bubbling is usually observed at the electrode.[5] The faster formation of the nonconducting gas phase increases the uncompensated resistance as well as the corresponding error of estimated R, resulting in significant uncertainties on iR-correction.[5] To avoid this possibility, our R was measured by EIS at open circuit potential, where no reaction takes place and no bubble forms. In addition, considering numerous publications perform iR-correction by EIS method, which is nearly a standard method, using EIS-derived R facilitates the readers to benchmark the catalyst against previous landmark studies.

Since alkaline solution causes the leaching of glass constituents into electrolyte, the electrochemical data collection was completed within 30 min since the initial exposure of electrolyte to the glass cell. Considering that the Cu- and Ni- containing NPs can be easily oxidized by the exposure to air, before the CV measurement, the working electrode was held at -0.1 V vs. RHE for 30 s to ensure the catalysts are metallic in nature, and then we immediately started HER measurement. The HER stability results are shown in Figure S25. The possible mechanism for performance loss is hydride formation, which is due to the hydrogen absorption caused by the strong bonding strength between Ni and H.[6] Such activity degradation has been commonly observed at Ni-based metal catalysts.[6] The stability issue is not further discussed, because this study aims at the activity descriptor, rather than stability investigation, which is interesting but beyond the scope of this study.

Measurement of surface composition and surface area of NiCu/C catalysts. The electrochemical active surface area (ECSA) of Ni and Cu at NiCu/C catalysts were measured by referencing the well-published methods in literatures.[7] The ECSA measurements were carried out in a one-compartment three-electrode cell, where a Pt foil served as counter electrode and a Hg/HgO electrode was used as reference electrode. All the CVs were scanned at a sweep rate of 20 mV/s in Ar-saturated 0.1 M KOH. Since the Cu- and Ni- containing NPs can be easily oxidized by the exposure to air, before the CV measurement, the working electrode was held at -0.1 V vs. RHE for 30 s to ensure the catalysts are metallic in nature, and then we immediately started conducting ECSA measurement.

The ECSA of Ni/C was measured by following a literature approach.[7-9] The CV was scanned from -0.15 V to 0.56 V vs. RHE. The ECSA of Ni was quantified by the reduction peak at ~0.05 V vs. RHE, which corresponds to the reduction of $Ni(OH)_2$ with a charge density of 514 $\mu C/cm^2_{Ni}$.

The ECSA of Cu/C was measured by following the literature approach[7, 10] with slight modifications. The CV was scanned from -0.15 V to 0.8 V vs. RHE. The ECSA of Cu was quantified by the anodic peak

at ~0.6 V vs. RHE, which corresponds to the formation of one monolayer of Cu_2O with a charge density of 360 μC/cm^2_{Cu}. In this work, we restricted the positive potential to 0.8 V vs. RHE (rather than 1.65 V vs. RHE, which has been used in previous studies) to avoid the danger that a too oxidizing potential might cause catalyst degradation. Our modification is rationalized by the fact that in the CV with a positive limit of 0.8 V vs. RHE, the peak for Cu ECSA quantification shows negligible difference from that measured by CV with a positive limit of 1.65 V vs. RHE (Figure S13a), indicating this modification does not affect the ECSA measurement. Another concern is the catalyst degradation caused by CV cycling. As evidenced by Figure S13b, the CV cycling decreases the intensity of the peak for Cu ECSA quantification (as well as the peak of Cu_2O reduction, ~0.35 V vs. RHE), indicating that the progressive occurrence of some irreversible structural changes. Therefore, for extracting the Cu ECSA, we use the 2nd CV cycle, which is still able to reflect the catalysts' original surface information.

The ECSA of NiCu/C catalysts was measured by the same approach as Cu/C. The CV was scanned from -0.15 V to 0.8 V vs. RHE, and to avoid catalyst degradation, the 2nd CV cycle was taken to extract surface area. The ECSA of Cu was quantified by the anodic peak at ~0.6 V vs. RHE, which corresponds to the formation of one monolayer of Cu_2O with a charge density of 360 μC/cm^2_{Cu}. The anodic peak (~0.35 V vs. RHE) at NiCu alloy is identified as the OH adsorption at Ni, as the peak position overlaps with that at pure Ni, which is consistent with the literature report; and at pure Cu, there is no peak around this potential range, which rules out the possibility that this peak originates from Cu. Since the OH desorption (reduction of $Ni(OH)_2$) peak at NiCu alloy is not discernible (masked by HER), the OH adsorption peak (~0.35 V vs. RHE) is alternatively used for Ni ECSA estimation, with the assumption that the charge density of 514 μC/cm^2_{Ni}, which equals that for OH desorption. Our modification is rationalized by the evidence that at pure Ni, the Coulombic charge under OH adsorption peak shows negligible difference from that of OH desorption. The surface area of NPs was estimated by totaling the Ni ECSA and Cu ECSA. The surface Ni coverage was estimated by normalizing Ni ECSA to the surface area of NPs.

To further prove that our approach for estimating the ECSA of NiCu/C, TEM method was used to calculate surface area of NPs. The surface area of NiCu NPs at NiCu/C was calculated according to the equation (assuming the particles are spherical and without internal porosity):[11]

$$Surface\ area\ = \frac{6 \times 10^3}{\rho * d}$$

where d is the average diameter (nm) of NiCu NPs from the size distribution histogram in Figure S3; ρ is the theoretic density (g/cm^3). The surface area of Ni measured with the aid of TEM is consistent with that estimated by the anodic peak of OH adsorption at CV, indicating that our approach for estimating Ni ECSA at NiCu/C is reliable.

ECSA measurement of Pt/C. The ECSA measurements were carried out in a one-compartment three-electrode cell (made of glassware), where a Pt foil served as counter electrode and a Hg/HgO electrode was used as reference electrode. The CV was firstly scanned from ~0.03 V to 1.1 V vs. RHE at a sweep rate of 50 mV/s in Ar-saturated 0.1 M KOH, which is for the purpose of cleaning the Pt surface. Afterwards, to determine the double-layer capacitive current, the positive potential window was restricted to 0.6 V vs. RHE to eliminate the interference from the reduction of Pt oxide. The CV measured with a positive vertex of 0.6 V vs. RHE is for quantifying ECSA.[7] The hydrogen adsorption/desorption region between 0.05 V and ~0.4 V vs. RHE (the onset of the double layer region) was used to calculate the Pt surface area, and the charge density for one monolayer of hydrogen coverage is 210 μC/cm^2_{Pt}.[7]

Density Functional Theory (DFT) calculation. All the density functional theory (DFT) calculations were performed by using Vienna Ab-initio Simulation Package (VASP)[12-13] under the Projected Augmented Wave (PAW)[14] method. The revised Perdew-Burke-Ernzerhof (RPBE) functional was used

to describe the exchange and correlation effects, since it has been proved to provide useful trend in computing adsorption energies.[15-17] In all the calculations, the cutoff energy was set to be 450 eV. The (111) surface was used to represent the catalytic interface of the metals and metal alloys. The Monkhorst-Pack grids[18] were set to be 4×4×1 and 9×9×1 for computing the surface optimizations and density of states (DOS) calculations, respectively. At least 18 Å vacuum layer was applied in z-direction of the slab models, preventing the slabs from vertical interactions.

The descriptor proposed by Norskov et al. was used to describe the HER activity on a given catalyst surface, where the free energy of hydrogen adsorption (ΔG_{H^*}) was considered as the key parameter determining the HER activity.[19] For HER in aqueous solutions, it is a two-step process and involves only one reaction intermediate, the chemisorbed H atom. The free energy of the adsorbed hydrogen is defined as:

$$\Delta G_{H^*} = \Delta E_H + \Delta E_{ZPE} - T\Delta S_H$$

where ΔE_H is the hydrogen binding energy, ΔE_{ZPE} is the zero-point energy difference between adsorbed hydrogen and gaseous hydrogen, and $T\Delta S$ is the corresponding entropy difference between these two states. According to previous studies,[19] here we used a 0.24 eV value to represent the correction of zero point energy and entropy of hydrogen state.

The NiCu alloy models were constructed in a face-centered-cubic (FCC) lattice frame with a 2×2×2 super cell, where Ni and Cu were arranged as randomly as possible to simulate a fully disordered mixture. During the optimizations, all the atoms were allowed to fully relax until the convergence criteria were reached. After achieving the optimized structure, the (111) surface was cleaved to represent the catalytic surface of NiCu alloys, as it is the most thermodynamically stable one in a FCC structure.[20]

Surface facet and strain analysis based on TEM characterization. The methodologies for analyzing the surface facet and strain are described as follows. High-resolution TEM images for individual particles are taken. For each particle, a region that is located at the surface is selected to perform fast Fourier transform (FFT). In the selected region, we search for the plane that fulfills two requirements: based on the FFT pattern, the direction of the plane is parallel to the edge (boundary) of the particle; based on the TEM image, the location of the plane overlaps with the edge (boundary) of the particle. The qualified plane is identified as the facet that is exposed; and then measured to get the d spacing, which is used for indexing the plane. To reveal the strain of each particle, a region that is located at the core is selected to perform FFT. Based on the acquired FFT pattern, the d spacing is measured. The comparison between the d spacing at the surface and core can reflect the strain of this particle.

The relationship between d band center and various surface structures. d band center is a parameter that cumulatively includes the influence from various surface structures such as strain and facet;[21] in other words, discussing the effect of d band center on HER has taken into consideration the facet and strain. Thus, to prove the descriptor role of d band center, it may not be necessary to reveal these surface structures. Here we detail the discussion to rationalize that the effect of strain, facet, particle size can be cumulatively described by d band center. The changes on these surface structures are cumulatively reflected on d band center. These surface structures shift the position of d band center toward or away from the Fermi level via altering the width of the d band.

We start from discussing that the effect of lattice strain can be explained by d band center. If a “small” metal atom is moved into the lattice of a “larger” one, the neighbors are further away and the d band width at the atom becomes smaller than that at the surface of the elemental metal. This leads to an up-shift of d band center in order to maintain the same d band filling locally. An example is the compression in the Pt shell at PtCu core-shell nanoparticles gives a higher ORR activity than

pure Pt, because the lattice compression in the shell shifts the d band center of Pt downward, which thereby weakens the adsorption energy of reactive intermediates compared to unstrained Pt.[22] Similarly, the superior CO oxidation performance of PtRu core-shell nanoparticles to pure Pt is attributed to a downshift in the d band center at the compressed Pt shell.[23] The fact that the strain effect is attributed to d band center can be also supported by the surface reactivity at Ru(0001), where the activity increases with lattice expansion, following a concurrent up-shift of d band center.[24] This correlation between strain and the movement of d band center is further supported by a landmark work,[25] which systematically studies the d band center at various combinations of 11 metals, including Fe, Co, Ni, Cu, Ru, Rh, Pd, Ag, Ir, Pt and Au. When one of these metals is alloyed into the surface of the other one or is deposited as a pseudomorphic overlayer at the other one, the d band center movement always correlates with strain; and the correlation follows the mechanism that the local d-band width are narrowed/widened and the center of the d band is caused to shift d band center up/down in order to preserve the degree of d-band filling.[25] More evidences about strain-induced shift of d band center at binary combinations of metal atoms can be found in ref [26]. Since the ligand effect is typically accompanied by strain, it has been difficult to separate the strain and ligand effects. One usually observes the cumulative effect of these two phenomena, which can be unified by one single parameter, i.e. d band center. This principle has been proved by a study at a series of bimetallic surface, i.e. the Ni, Pd and Pt monolayers supported on various transition metals.[27] The changes in hydrogen adsorption energy at these bimetallic surfaces due to the combined strain and ligand effects is traced to changes of d band center.[27]

The changes on facet is reflected by d band center. The d band center can be varied for a specific transition metal by varying the structure. Various facets consist of metals with varied coordination number, which leads to the substantial variations in the d band centers.[28] The atoms in the most close-packed (111) surface of Pt have a coordination number of 9. In the more open (100) surface it is 8 and at a step or at the (110) surface it is 7. At a kink the coordination number is as low as 6.[28-29] As shown in the earlier, this leads to variations in the d-band center of almost 1 eV, and the chemisorption energy of CO varies by a similar fashion.[28-29] The fact that step surfaces bind CO stronger than the flat surfaces is in excellent agreement with experimental evidence, and it is explained by d band theory.[29] The various Pt facets possess different activities of oxygen reduction reaction, which are also correlated with the d band center.[30] The facet-induced d band center variation is also reported at other metals, including Ni and Cu. Due to the higher position of d band center at stepped Ni(211) surface than flat (111), the adsorption at Ni(211) is stronger than (111).[21] Among Cu (111), (100) and (211), the difference of the d band center is about 0.2 eV, and the highest for the (211) and lowest for (111).[31] This is consistent with the observed order of the binding energies, which shows variations in the adsorption strength of a similar magnitude, indicating that the effect of facet is governed by the effect of d band center.[31]

The surface structure variations led by the change of particle size are associated with d band center. If the particle size decreases, it generates surface structures such as stepped surfaces, under-coordinated atoms (atoms that have a smaller coordination number), defects; and the portion of planar, and terrace surfaces becomes less. As the coordination number varies the d band center (mentioned in the earlier paragraph), the decreasing particle size moves the d band center upward.[29] A classic example is the size effect of Pt metal on oxygen reduction reaction: the smaller the particle size, the lower the specific activity of oxygen reduction reaction is.[32-33] This is consistent with the d band theory: since the O adsorption at bulk Pt is slightly stronger than the optimum value, a smaller particle size moves the d band center toward Fermi level and enhances the O adsorption, and thus decreasing the activity.[32] Similarly, since the adsorption strength at bulk Au is too weak, decreasing

the particle size of Au moves the d band center upward and enhances the adsorption ability; as a result, the surface reactivity of Au increases.[34]

To sum up, the above discussion validates that the d band center is a parameter that cumulatively includes the influence from various surface structures such as strain, facet, under-coordinated atoms. To further rationalize this discussion (and as a summary of this discussion), we cite the conclusion from a landmark study that simultaneously correlates a significant number of these surface structural effects with d band center.[21] It has been proved that the d band center can be used to quantitatively predict trends on a variety of surfaces with different geometries, strain levels, promoters, poisons, and alloy compositions. The d band center has a general descriptive power.

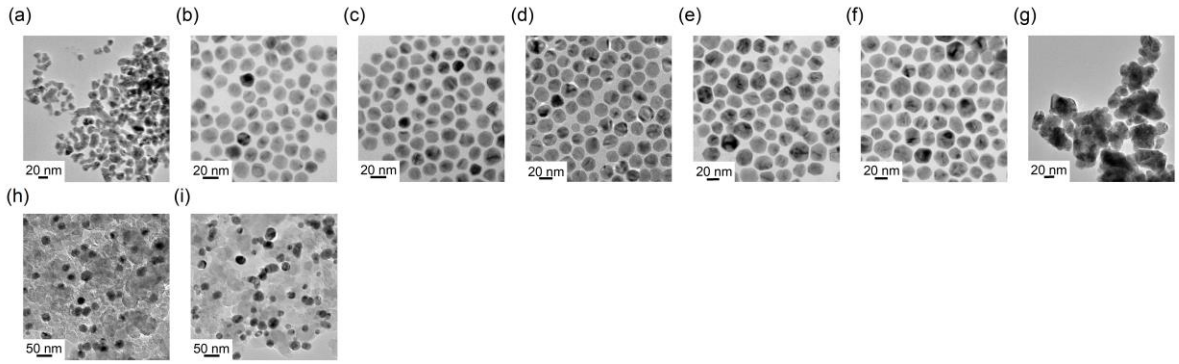

Figure S1. TEM images of free-standing NiCu NPs: (a) Cu, (b) Ni_1Cu_3, (c) Ni_1Cu_2, (d) Ni_1Cu_1, (e) Ni_2Cu_1, (f) Ni_3Cu_1, (g) Ni. TEM images of (h) Cu/C and (i) Ni/C (loaded on carbon, after heat treatment). Considering that the free-standing Ni and Cu NPs (before carbon loading) were agglomerated and spiky, the TEM observation indicates that the long-term sonication during carbon loading had well separated the NPs; and the heat-treatment shaped NPs into spherical morphology.

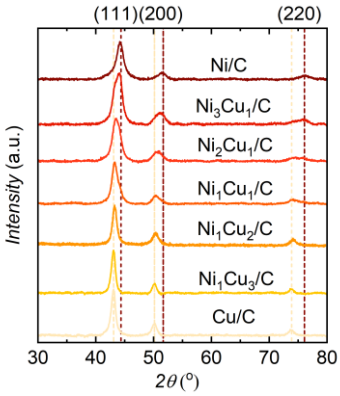

Figure S2. XRD patterns of NiCu/C catalysts after heat treatment.

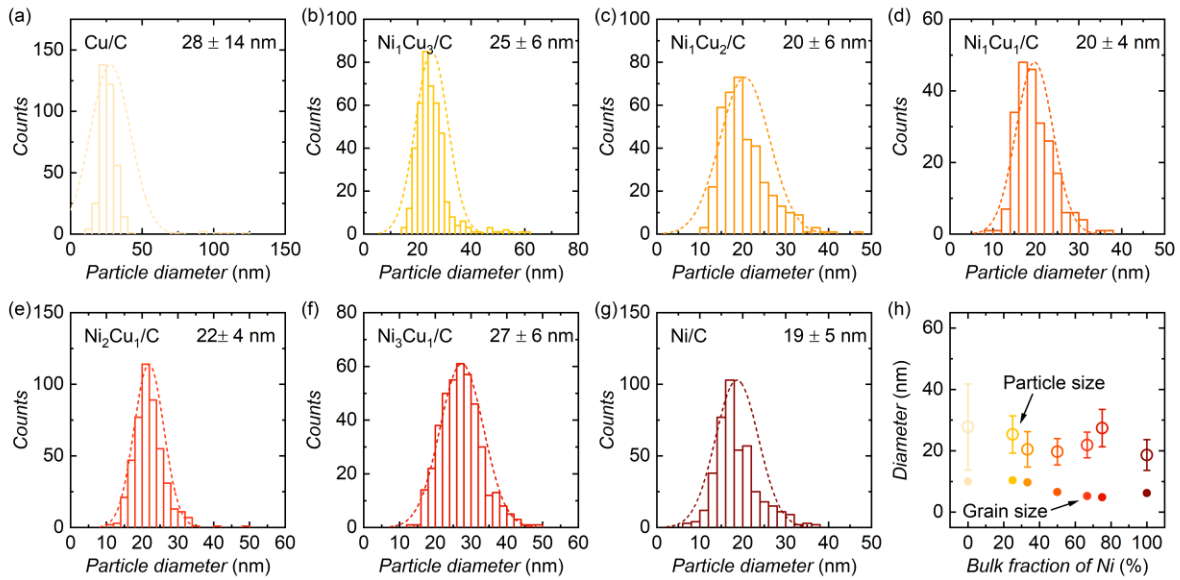

Figure S3. (a - g) The histograms of particle diameter measured from > 250 NPs at TEM images. (h) The average diameter (open circles) as a function of bulk fraction Ni. The grain size (filled circles) estimated by XRD with Scherrer equation. The error bars are derived from the statistical analysis.

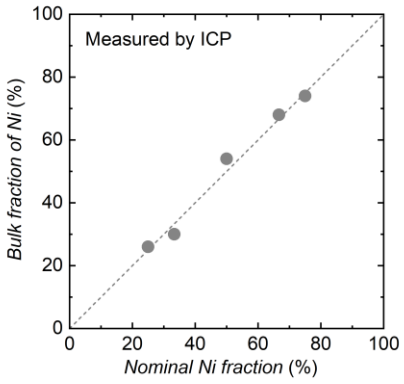

Figure S4. The particle composition (bulk fraction Ni) measured by Inductively Coupled Plasma (ICP) as a function the nominal Ni fraction (precursor feeding ratio). The plot shows that the particle composition is consistent with the nominal Ni fraction.

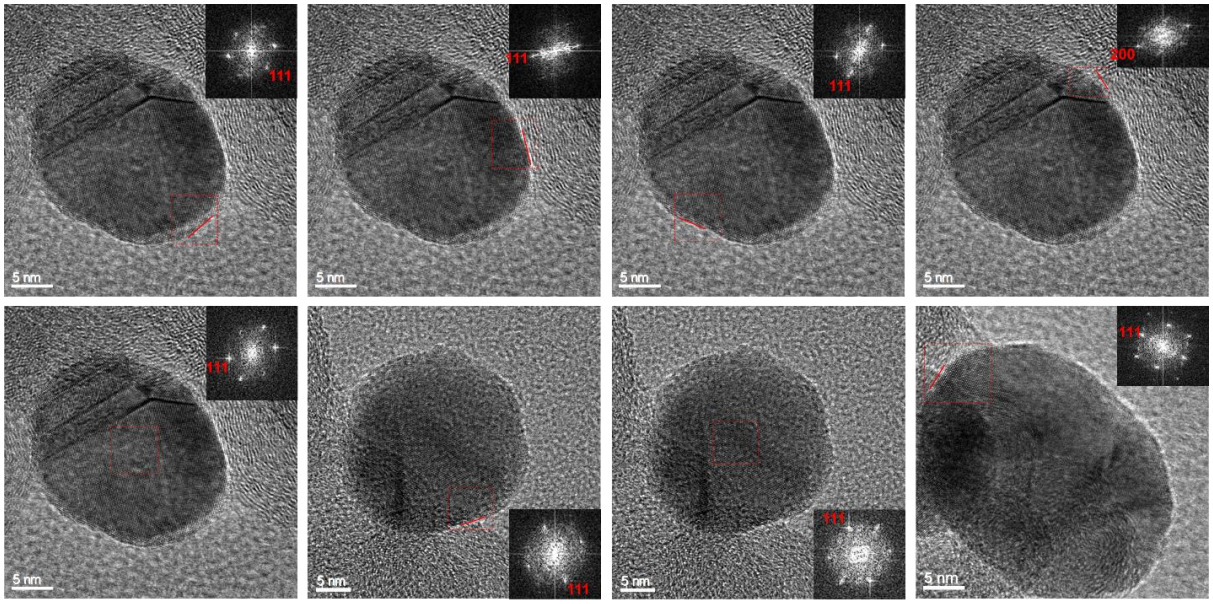

Figure S5. The demonstration of surface analysis at Ni_1Cu_3/C catalysts. The red dash line box is the selected region for FFT analysis. The red solid line labels the exposed facet.

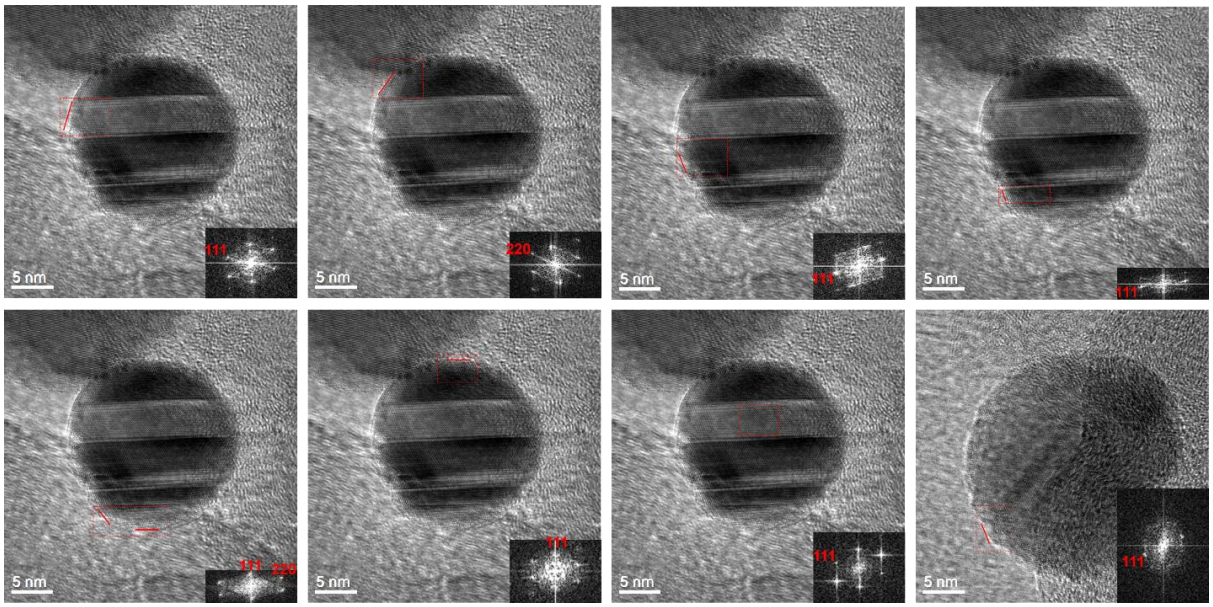

Figure S6. The demonstration of surface analysis at Ni_1Cu_2/C catalysts. The red dash line box is the selected region for FFT analysis. The red solid line labels the exposed facet.

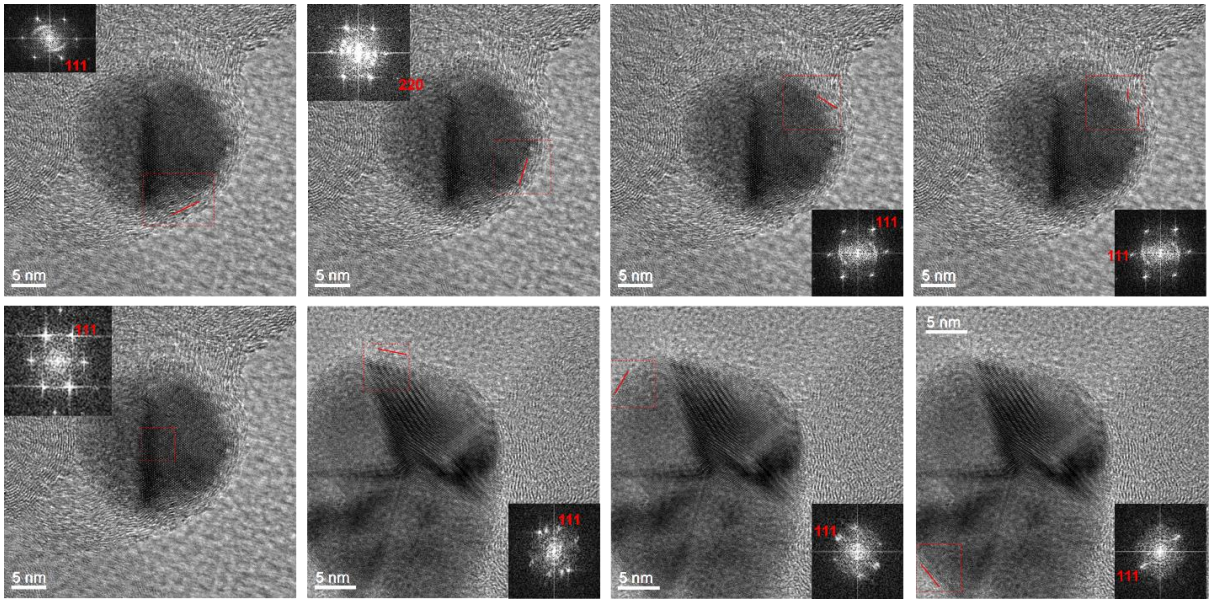

Figure S7. The demonstration of surface analysis at Ni_1Cu_1/C catalysts. The red dash line box is the selected region for FFT analysis. The red solid line labels the exposed facet.

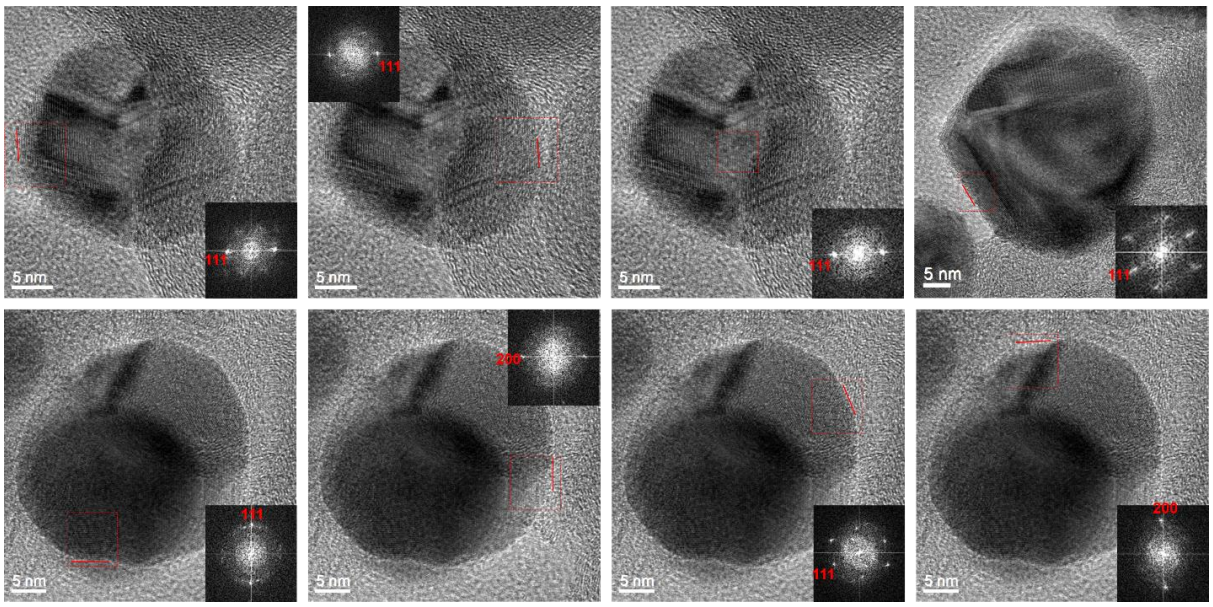

Figure S8. The demonstration of surface analysis at Ni_2Cu_1/C catalysts. The red dash line box is the selected region for FFT analysis. The red solid line labels the exposed facet.

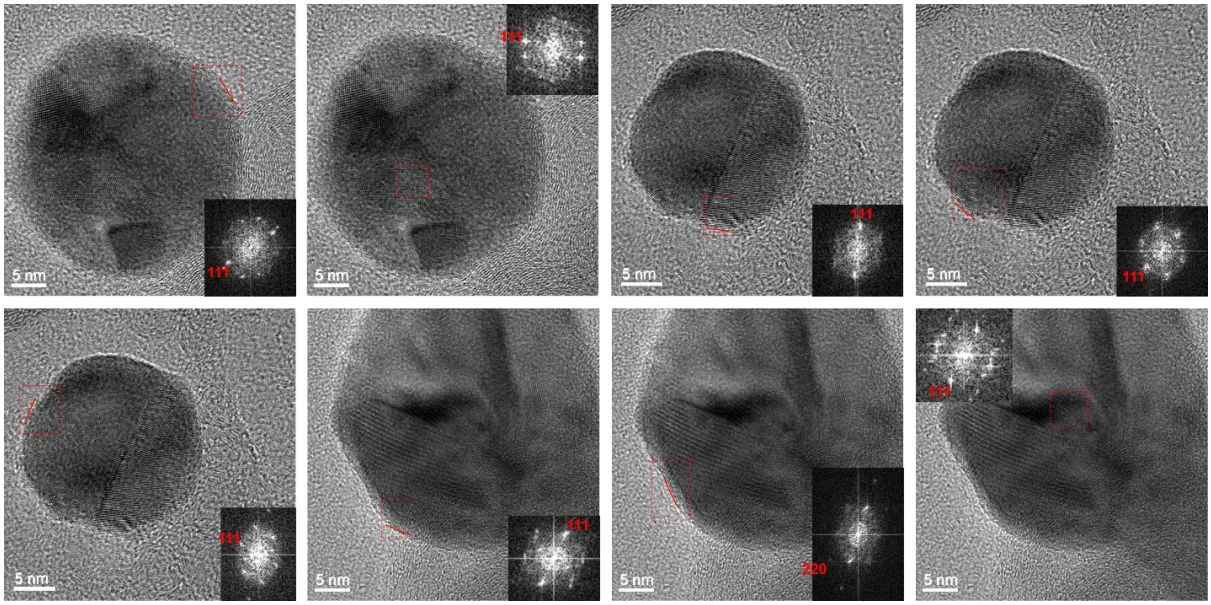

Figure S9. The demonstration of surface analysis at Ni_3Cu_1/C catalysts. The red dash line box is the selected region for FFT analysis. The red solid line labels the exposed facet.

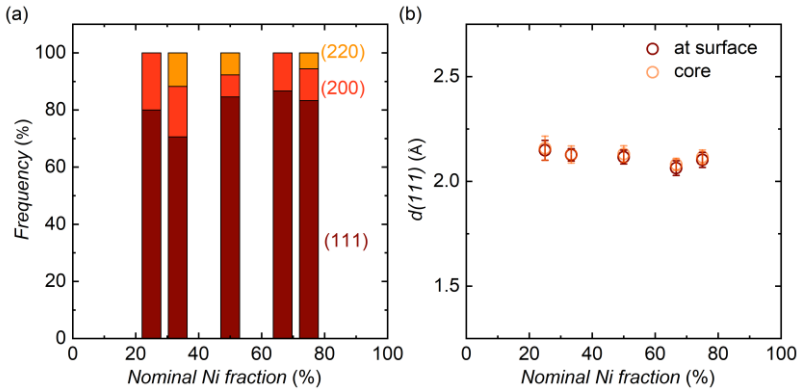

Figure S10. The summary of (a) exposed facets and (b) d spacing of (111) plane at NiCu bimetallic with various compositions. Data is acquired by analyzing TEM images.

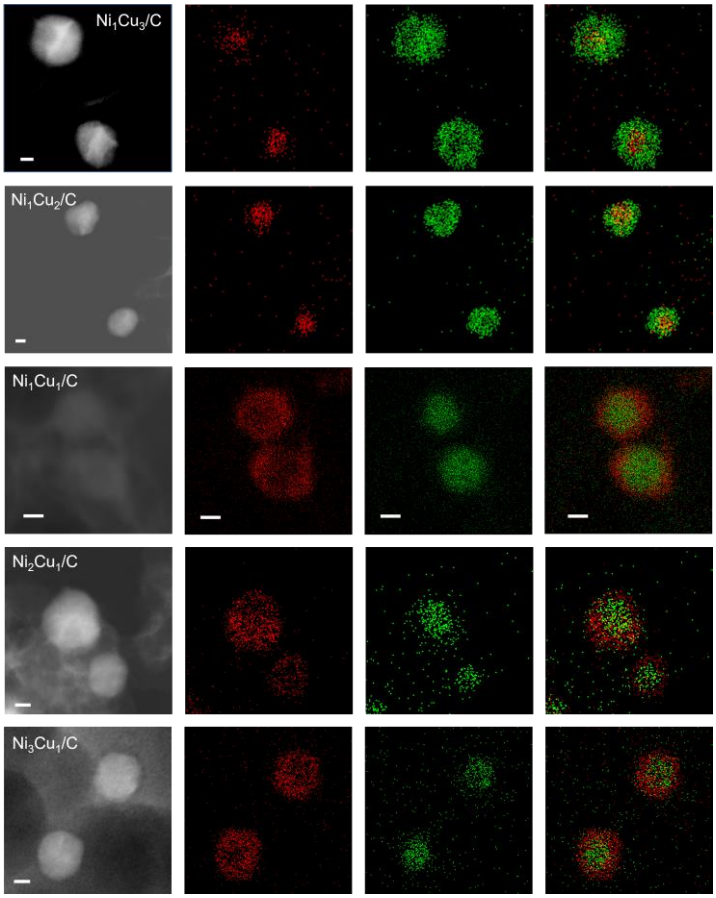

Figure S11. TEM-EDS mapping at NiCu/C (after heat treatment) with various compositions. The scale bars are 10 nm. Red color refers to Ni and green is Cu.

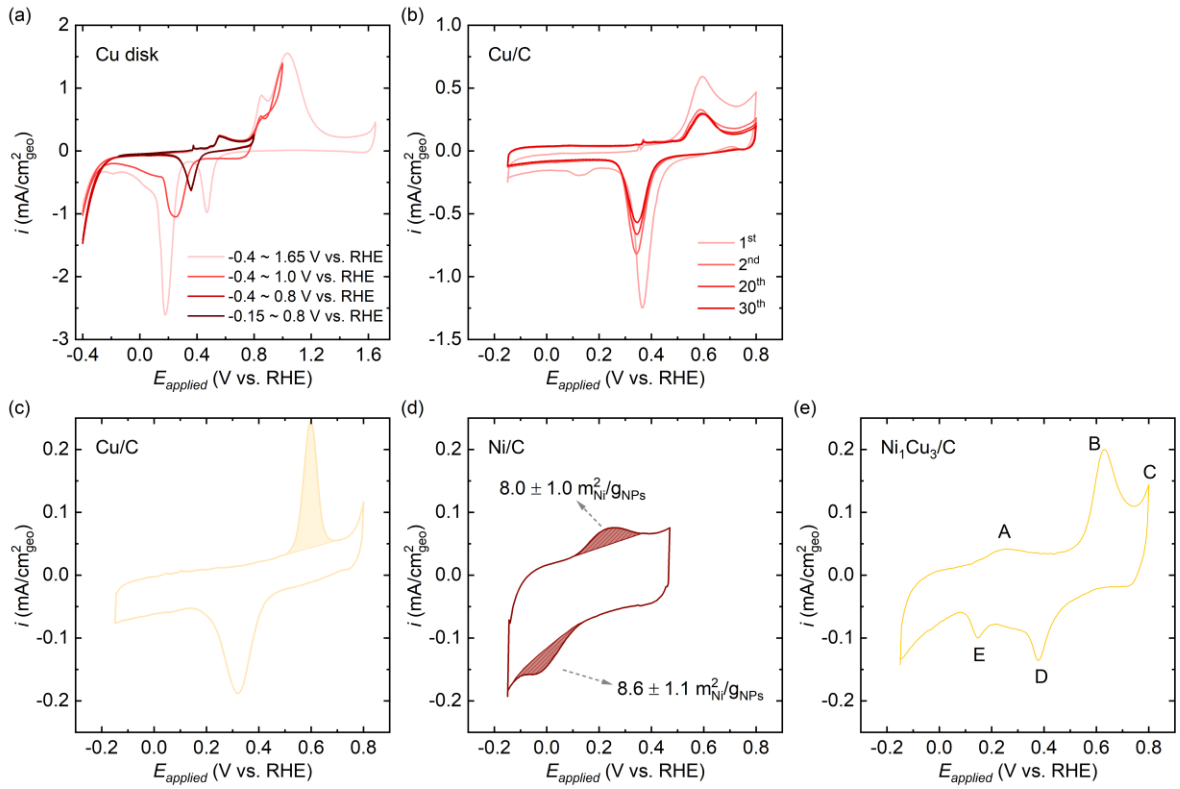

Figure S12. (a) CV of Cu disk with various positive/negative limit potentials. (b) CV of Cu/C at different cycle number. (c) The demonstration of the peak integration at Cu/C for the quantification of Cu ECSA. (d) The demonstrate of the peak integration at Ni/C for the quantification of Ni ECSA. It indicates that the surface area estimated by the anodic peak for OH adsorption and that by the cathodic peak of OH desorption are consistent. CVs were collected in Ar-saturated 0.1 M KOH at the scan rate of 20 mV/s. (e) The processes under each peak are detailed with Ni_1Cu_3/C as an example. A denotes the oxidation of Ni to $Ni(OH)_2$; B is the formation of the first Cu_2O monolayer; C is the formation of the second Cu_2O monolayer; D is the reduction of the first Cu_2O monolayer; E is the reduction of the second Cu_2O monolayer. On the basis of the results from Ni surfaces in literature[7-9] and our NiCu bimetallic surfaces, it is inferred that the reduction peak of $Ni(OH)_2$ is possibly mixed with the reduction of Cu_2O monolayer, and concealed under peak E.

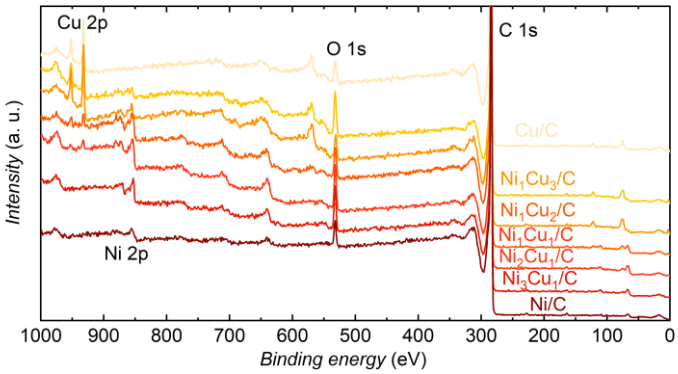

Figure S13. XPS survey spectra of NiCu/C catalysts. The trends in Ni 2p and Cu 2p peaks show the compositional variation of these catalysts.

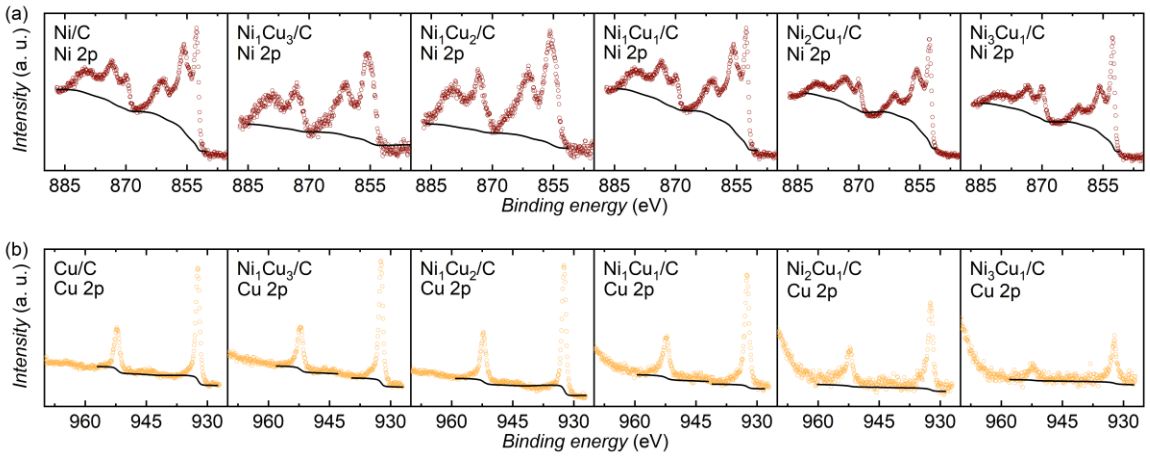

Figure S14. (a) Ni 2p and (b) Cu 2p XPS spectra at various NiCu/C catalysts. The Shirley-type baseline for peak integration is indicated by solid black line.

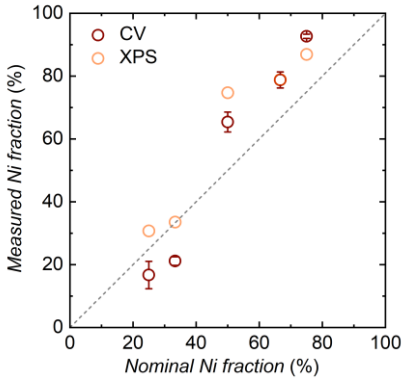

Figure S15. The Ni fraction measured by CV and XPS at various NiCu/C catalysts.

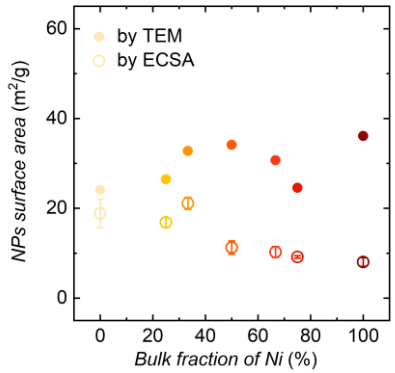

Figure S16. The surface areas of NiCu NPs estimated by TEM and ECSA method. The error bars represent at least three independent measurements.

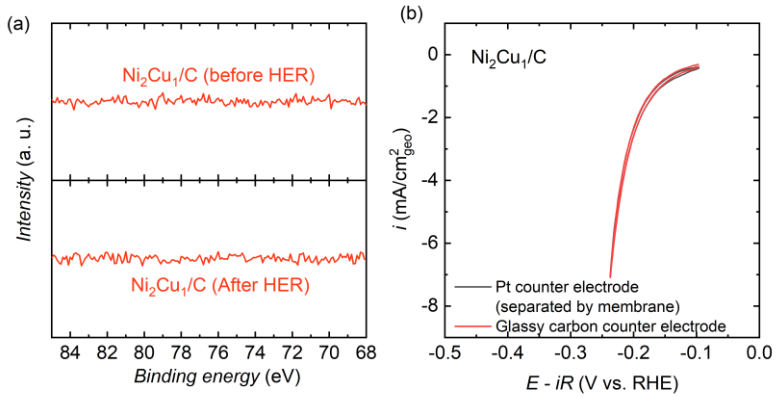

Figure S17. (a) The Pt signal is not detected by XPS after the HER measurement, which demonstrates that by separating working and counter electrode compartment, our HER measurement does not involve Pt contamination caused by the use of Pt counter electrode. The Pt $4f_{5/2}$ and $4f_{7/2}$ peaks should locate at 74.4 and 71.3 eV, respectively.[35] (b) The CV at Ni_2Cu_1/C measured by our setup (Pt counter electrode, and anion exchange membrane) is the same as that measured with glassy carbon (which does not contain Pt) as the counter electrode. This rules out the interference from Pt contamination in our HER measurement. In addition, after the measurement with our setup, the electrolyte in the working electrode compartment is analyzed by ICP, which does not detect Pt.

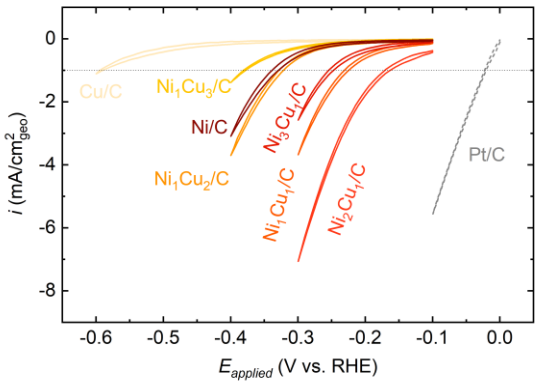

Figure S18. The exemplary CVs of NiCu/C catalysts with various compositions. CVs were collected with a scan rate of 10 mV/s and a rotation speed of 1600 rpm in H_2-saturated 0.1 M KOH at 25 °C. The potential axis was not iR corrected, and the current density was normalized to the geometric area of the glassy carbon electrode. Considering that the Cu- and Ni- containing NPs can be easily oxidized by the exposure to air, before the CV measurement, the working electrode was held at -0.1 V vs. RHE for 30 s to ensure the catalysts are metallic in nature, and then we immediately started HER measurement.

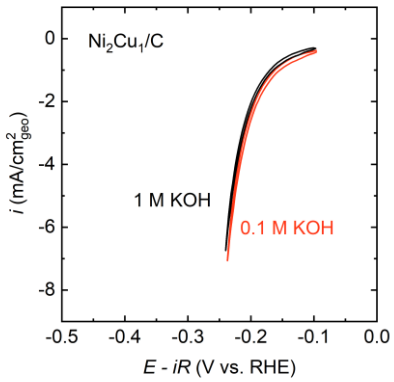

Figure S19. The iR-corrected CVs of Ni_2Cu_1/C catalysts collected with a scan rate of 10 mV/s and a rotation speed of 1600 rpm in H_2-saturated 0.1 M KOH and 1.0 M KOH at 25 °C. As revealed in the previous study, the local acid-like environment has been only observed at Pt nanoparticles with diameters of < 5 nm; bulk Pt catalyst does not show such behavior.[36] Thus, the absence of such observation in our study might be due to the fact that our particle size is not sufficiently small: our particle diameter is ~20 nm and that in the reference is < 5 nm. As evidenced by a size effect study,[33] the nanoparticles with diameters > 10 nm show electrochemical performance similar to bulk materials. It is therefore inferred that our particles, (which are ~ 20 nm), might exhibit the properties that are similar to bulk materials (e.g. bulk Pt), which do not show the local acid-like behavior.

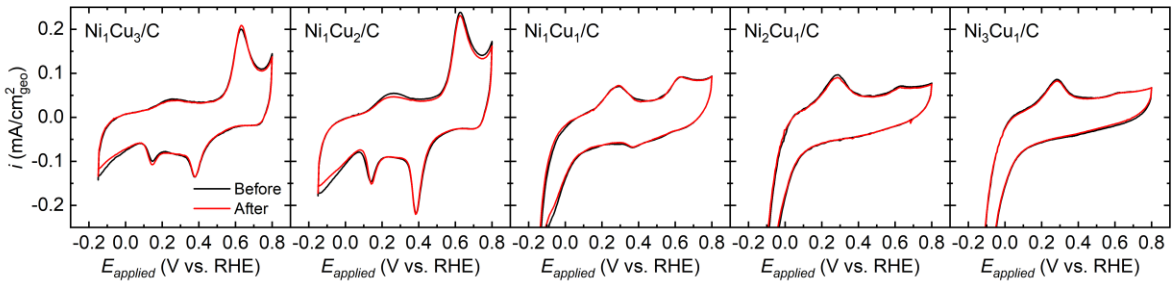

Figure S20. The CVs of various NiCu/C catalysts after 10 cycles of HER measurement. The results (see the figure below) show that the CV before and after HER measurement (10 cycles) almost overlap, indicating that the Ni:Cu ratio keeps unchanged during the HER measurement. This validates our established correlation between HER activity and surface-composition-dependent electronic structure. The CVs were collected in Ar-saturated 0.1 M KOH at the scan rate of 20 mV/s.

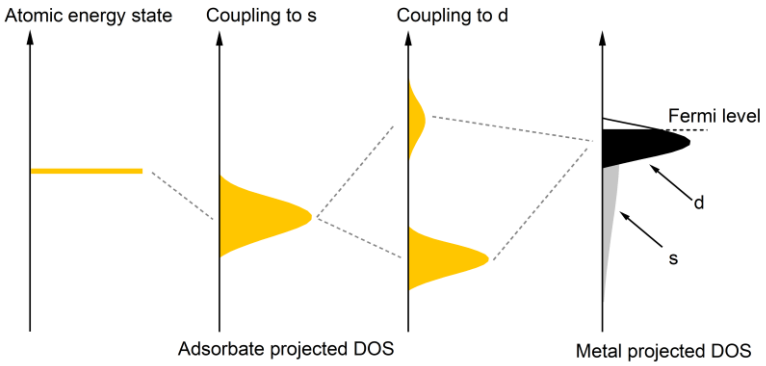

Figure S21. Schematic illustration of the interaction between an adsorbate valence level and the delocalized s-states and localized d-states of a transition metal surface.

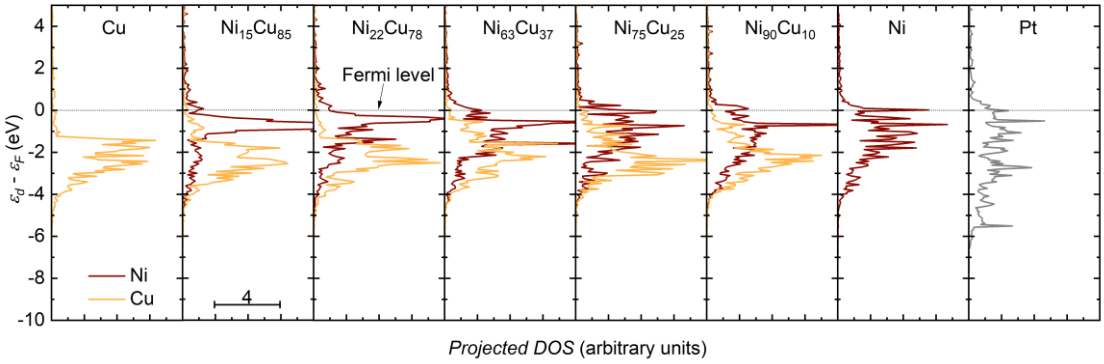

Figure S22. Calculated d-projected densities of states (DOS) of Ni and Cu site at NiCu alloy surfaces with various compositional fraction of Ni atoms. The d band DOS of Pt surface is shown as a reference. Dashed lines indicate the fermi level.

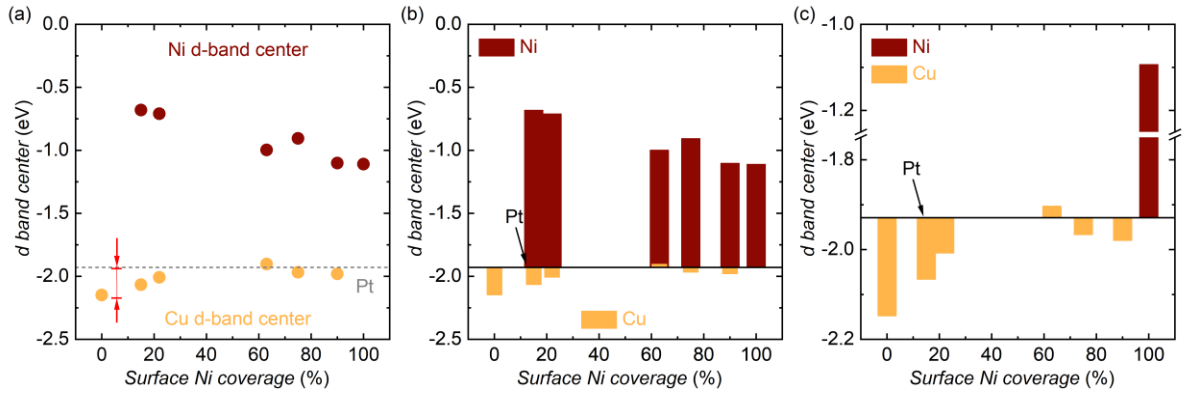

Figure S23. (a) The calculated position d band centers relative to Fermi level at NiCu alloy with various Ni fractions. The d band center of Ni ($\varepsilon_{d\text{-}Ni}$) at NiCu alloy (red colour dots) and the d band center of Cu ($\varepsilon_{d\text{-}Cu}$) at NiCu alloy (yellow colour dots). The dash line is the d band center position of Pt ($\varepsilon_{d\text{-}Pt}$). (b) is the same data as panel (a), but panel (b) is shown in the forms of columns. The column height represents the distance between the d band center of Ni/Cu and that of Pt (indicated by the red arrow in panel (a)). (c)The d band center at the active site of each NiCu alloy.

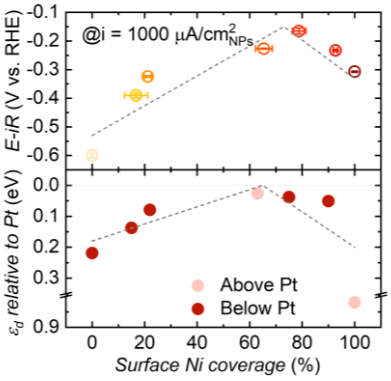

Figure S24. Top panel is the measured HER activity (defined as the potential at 1000 $\mu A/cm^2_{NPs}$) versus surface Ni coverage (estimated by ECSA). The grey dash line is drawn to guide the readers. The error bars represent at least three independent measurements. Bottom panel is the d band center (ε_d) relative to Pt (which reflects HER activity) versus the Ni fraction used in DFT calculation. The d band center relative to Pt at NiCu alloy (except for Ni) is taken as the distance between the d band center of Cu and that of Pt. The volcano-shaped grey dash line is drawn to guide the readers. The d band center (ε_d) relative to Pt is calculated by $\varepsilon_d - \varepsilon_{d\text{-}Pt}$. The horizontal dotted line represents the distance relative to Pt is zero. The consistency between these two trends in top and bottom panel suggests that d band center is the governing factor of HER activity of various NiCu/C catalysts in alkaline.

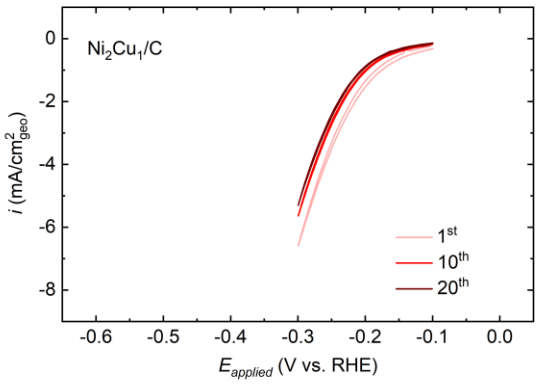

Figure S25. The exemplary HER stability test at Ni_2Cu_1/C catalyst. CVs (from 1st to 20th cycle) were collected with a scan rate of 10 mV/s and a rotation speed of 1600 rpm in H_2-saturated 0.1 M KOH at 25 °C. The potential axis was not iR corrected, and the current density was normalized to the geometric area of the glassy carbon electrode.

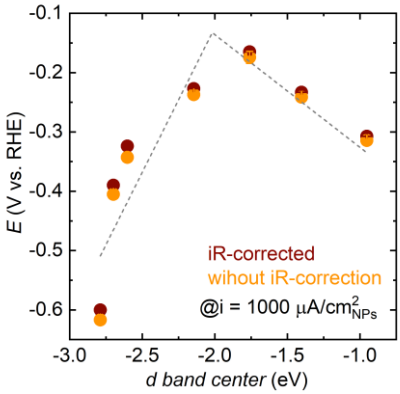

Figure S26. HER specific activity (defined as the potential at 1000 μA/cm^2_{NPs}) of various NiCu/C catalysts as a function of d band center. The d band center is estimated by XPS measurement. Both the iR-corrected activity and the activity without iR-correction are shown to demonstrate that iR-correction does not affect our established trend of activity vs. d band center.

Table S1. The summary of the DFT model for each NiCu/C catalyst. Hydrogen binding energy (ΔG_H) at the hollow site of the selected NiCu/C catalysts.

Catalyst	**DFT model**	**ΔG_H (eV)**
Cu/C	Cu	0.22
Ni_1Cu_3/C	$Ni_{15}Cu_{85}$	
Ni_1Cu_2/C	$Ni_{22}Cu_{78}$	
Ni_1Cu_1/C	$Ni_{63}Cu_{78}$	-0.16
Ni_2Cu_1/C	$Ni_{75}Cu_{78}$	-0.12
Ni_3Cu_1/C	$Ni_{90}Cu_{78}$	
Ni/C	Ni	-0.27
Pt	Pt	-0.09

References

(1) Hofmann, T.; Yu, T. H.; Folse, M.; Weinhardt, L.; Bär, M.; Zhang, Y.; Merinov, B. V.; Myers, D. J.; Goddard, W. A.; Heske, C., Using Photoelectron Spectroscopy and Quantum Mechanics to Determine d-Band Energies of Metals for Catalytic Applications. *J. Phys. Chem. C* **2012,** *116*, 24016-24026.
(2) Wei, C.; Rao, R. R.; Peng, J.; Huang, B.; Stephens, I. E. L.; Risch, M.; Xu, Z. J.; Shao-Horn, Y., Recommended Practices and Benchmark Activity for Hydrogen and Oxygen Electrocatalysis in Water Splitting and Fuel Cells. *Adv. Mater.* **2019,** *31*, 1806296.
(3) Hong, W. T.; Risch, M.; Stoerzinger, K. A.; Grimaud, A.; Suntivich, J.; Shao-Horn, Y., Toward the rational design of non-precious transition metal oxides for oxygen electrocatalysis. *Energy Environ. Sci.* **2015,** *8*, 1404-1427.
(4) Cooper, K. R.; Smith, M., Electrical test methods for on-line fuel cell ohmic resistance measurement. *J. Power Sources* **2006,** *160*, 1088-1095.
(5) Čolić, V.; Tymoczko, J.; Maljusch, A.; Ganassin, A.; Schuhmann, W.; Bandarenka, A. S., Experimental Aspects in Benchmarking of the Electrocatalytic Activity. *ChemElectroChem* **2015,** *2*, 143-149.
(6) Tang, M. H.; Hahn, C.; Klobuchar, A. J.; Ng, J. W. D.; Wellendorff, J.; Bligaard, T.; Jaramillo, T. F., Nickel-silver alloy electrocatalysts for hydrogen evolution and oxidation in an alkaline electrolyte. *Phys. Chem. Chem. Phys.* **2014,** *16*, 19250-19257.
(7) Sheng, W.; Myint, M.; Chen, J. G.; Yan, Y., Correlating the hydrogen evolution reaction activity in alkaline electrolytes with the hydrogen binding energy on monometallic surfaces. *Energy Environ. Sci.* **2013,** *6*, 1509-1512.
(8) Conway, B. E.; Bai, L., Determination of the adsorption behaviour of 'overpotential-deposited' hydrogen-atom species in the cathodic hydrogen-evolution reaction by analysis of potential-relaxation transients. *J. Chem. Soc., Faraday Trans. 1* **1985,** *81*, 1841-1862.
(9) Machado, S. A. S.; Avaca, L. A., The hydrogen evolution reaction on nickel surfaces stabilized by H-absorption. *Electrochim. Acta* **1994,** *39*, 1385-1391.
(10) Fletcher, S.; Barradas, R. G.; Porter, J. D., The Anodic Oxidation of Copper Amalgam and Polycrystalline Copper Electrodes in LiOH Solution. *J. Electrochem. Soc.* **1978,** *125*, 1960-1968.
(11) Wei, C.; Sun, S.; Mandler, D.; Wang, X.; Qiao, S. Z.; Xu, Z. J., Approaches for measuring the surface areas of metal oxide electrocatalysts for determining their intrinsic electrocatalytic activity. *Chem. Soc. Rev.* **2019,** *48*, 2518-2534.
(12) Kresse, G.; Furthmüller, J., Efficient iterative schemes for ab initio total-energy calculations using a plane-wave basis set. *Phys. Rev. B* **1996,** *54*, 11169-11186.
(13) Kresse, G.; Hafner, J., Ab initio molecular-dynamics simulation of the liquid-metal--amorphous-semiconductor transition in germanium. *Phys. Rev. B* **1994,** *49*, 14251-14269.
(14) Blöchl, P. E., Projector augmented-wave method. *Phys. Rev. B* **1994,** *50*, 17953-17979.
(15) Perdew, J. P.; Burke, K.; Ernzerhof, M., Generalized Gradient Approximation Made Simple. *Phys. Rev. Lett.* **1996,** *77*, 3865-3868.
(16) Zhang, Y.; Yang, W., Comment on ``Generalized Gradient Approximation Made Simple''. *Phys. Rev. Lett.* **1998,** *80*, 890-890.
(17) Hammer, B.; Hansen, L. B.; Nørskov, J. K., Improved adsorption energetics within density-functional theory using revised Perdew-Burke-Ernzerhof functionals. *Phys. Rev. B* **1999,** *59*, 7413-7421.
(18) Monkhorst, H. J.; Pack, J. D., Special points for Brillouin-zone integrations. *Phys. Rev. B* **1976,** *13*, 5188-5192.
(19) Nørskov, J. K.; Bligaard, T.; Logadottir, A.; Kitchin, J. R.; Chen, J. G.; Pandelov, S.; Stimming, U., Trends in the Exchange Current for Hydrogen Evolution. *J. Electrochem. Soc.* **2005,** *152*, J23-J26.
(20) Li, Z.; Wang, S.; Chin, W. S.; Achenie, L. E.; Xin, H., High-throughput screening of bimetallic catalysts enabled by machine learning. *J. Mater. Chem. A* **2017,** *5*, 24131-24138.
(21) Abild-Pedersen, F.; Greeley, J.; Nørskov, J. K., Understanding the Effect of Steps, Strain, Poisons, and Alloying: Methane Activation on Ni Surfaces. *Catal. Lett.* **2005,** *105*, 9-13.

(22) Strasser, P.; Koh, S.; Anniyev, T.; Greeley, J.; More, K.; Yu, C.; Liu, Z.; Kaya, S.; Nordlund, D.; Ogasawara, H.; Toney, M. F.; Nilsson, A., Lattice-strain control of the activity in dealloyed core–shell fuel cell catalysts. *Nat. Chem.* **2010,** *2*, 454-460.
(23) Alayoglu, S.; Nilekar, A. U.; Mavrikakis, M.; Eichhorn, B., Ru–Pt core–shell nanoparticles for preferential oxidation of carbon monoxide in hydrogen. *Nat. Mater.* **2008,** *7*, 333-338.
(24) Mavrikakis, M.; Hammer, B.; Nørskov, J. K., Effect of Strain on the Reactivity of Metal Surfaces. *Phys. Rev. Lett.* **1998,** *81*, 2819-2822.
(25) Ruban, A.; Hammer, B.; Stoltze, P.; Skriver, H. L.; Nørskov, J. K., Surface electronic structure and reactivity of transition and noble metals1Communication presented at the First Francqui Colloquium, Brussels, 19–20 February 1996.1. *Journal of Molecular Catalysis A: Chemical* **1997,** *115*, 421-429.
(26) Christoffersen, E.; Liu, P.; Ruban, A.; Skriver, H. L.; Nørskov, J. K., Anode Materials for Low-Temperature Fuel Cells: A Density Functional Theory Study. *J. Catal.* **2001,** *199*, 123-131.
(27) Kitchin, J. R.; Nørskov, J. K.; Barteau, M. A.; Chen, J. G., Role of Strain and Ligand Effects in the Modification of the Electronic and Chemical Properties of Bimetallic Surfaces. *Phys. Rev. Lett.* **2004,** *93*, 156801.
(28) Hammer, B.; Nielsen, O. H.; Nrskov, J. K., Structure sensitivity in adsorption: CO interaction with stepped and reconstructed Pt surfaces. *Catal. Lett.* **1997,** *46*, 31-35.
(29) Bligaard, T.; Nørskov, J. K., Ligand effects in heterogeneous catalysis and electrochemistry. *Electrochim. Acta* **2007,** *52*, 5512-5516.
(30) Stamenkovic, V. R.; Fowler, B.; Mun, B. S.; Wang, G.; Ross, P. N.; Lucas, C. A.; Markovic, N. M., Improved oxygen reduction activity on Pt3Ni(111) via increased surface site availability. *Science* **2007,** *315*, 493-497.
(31) Durand, W. J.; Peterson, A. A.; Studt, F.; Abild-Pedersen, F.; Nørskov, J. K., Structure effects on the energetics of the electrochemical reduction of CO2 by copper surfaces. *Surf. Sci.* **2011,** *605*, 1354-1359.
(32) Toyoda, E.; Jinnouchi, R.; Hatanaka, T.; Morimoto, Y.; Mitsuhara, K.; Visikovskiy, A.; Kido, Y., The d-Band Structure of Pt Nanoclusters Correlated with the Catalytic Activity for an Oxygen Reduction Reaction. *J. Phys. Chem. C* **2011,** *115*, 21236-21240.
(33) Perez-Alonso, F. J.; McCarthy, D. N.; Nierhoff, A.; Hernandez-Fernandez, P.; Strebel, C.; Stephens, I. E. L.; Nielsen, J. H.; Chorkendorff, I., The Effect of Size on the Oxygen Electroreduction Activity of Mass-Selected Platinum Nanoparticles. *Angew. Chem., Int. Ed.* **2012,** *51*, 4641-4643.
(34) Phala, N. S.; van Steen, E., Intrinsic reactivity of gold nanoparticles: Classical, semi-empirical and DFT studies. *Gold. Bull.* **2007,** *40*, 150-153.
(35) Sheng, W.; Chen, S.; Vescovo, E.; Shao-Horn, Y., Size Influence on the Oxygen Reduction Reaction Activity and Instability of Supported Pt Nanoparticles. *J. Electrochem. Soc.* **2012,** *159*, B96-B103.
(36) Wang, X.; Xu, C.; Jaroniec, M.; Zheng, Y.; Qiao, S.-Z., Anomalous hydrogen evolution behavior in high-pH environment induced by locally generated hydronium ions. *Nat. Commun.* **2019,** *10*, 4876-4883.